Molecular Cell

Article

MEDAG functions as an A-kinase-anchoring protein in adipocytes

Graphical abstract

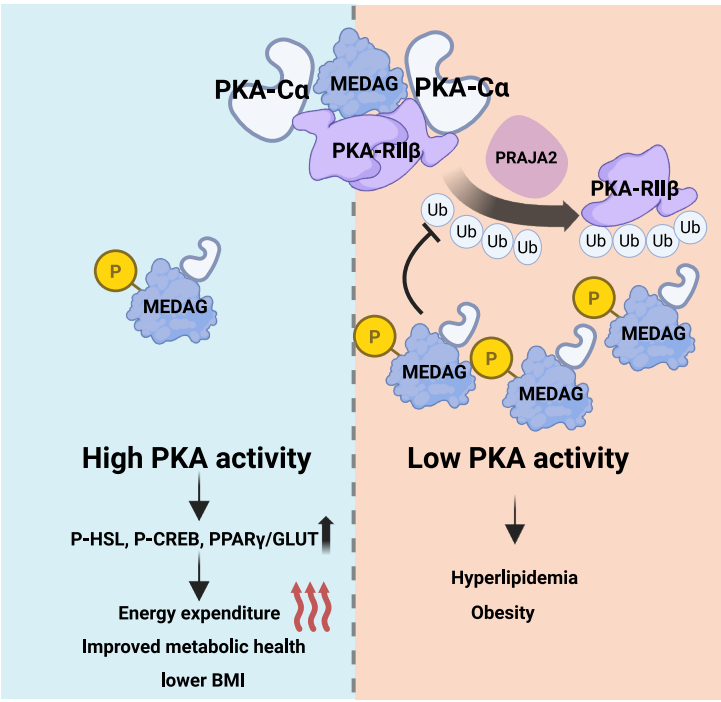

Highlights

- Adipose MEDAG expression correlates with obesity and moderates adipocyte catabolism
- MEDAG interacts with and regulates PKA-RIIβ
- MEDAG and PKA form an autoregulatory phosphorylation loop that fine-tunes PKA activity
- Adipocyte *Medag* loss mitigates diet-induced obesity via increased energy expenditure

Authors

Fen Long, Adhideb Ghosh, Tianyu Xu, ..., Miroslav Balaz, Anand Kumar Sharma, Christian Wolfrum

Correspondence

a.sharma2@imperial.ac.uk (A.K.S.), christian.wolfrum@ntu.edu.sg (C.W.)

In brief

Long et al. demonstrate that MEDAG functions as an A-kinase anchoring protein in adipocytes by interacting with and regulating PKA-RIIβ, thereby tuning PKA activity. *Medag* deletion elevates adipose energy expenditure, suggesting MEDAG as a potential target to increase energy dissipation.

Long et al., 2026, Molecular Cell *86*, 937–953
March 5, 2026
https://doi.org/10.1016/j.molcel.2026.02.001

CellPress

Molecular Cell

CellPress
OPEN ACCESS

Article

MEDAG functions as an A-kinase-anchoring protein in adipocytes

Fen Long,[1] Adhideb Ghosh,[1] Tianyu Xu,[2] Lianggong Ding,[1] Chunyan Wu,[1] Radhika Khandelwal,[1] Falko Noé,[1] Wenfei Sun,[3] Hua Dong,[4] Tongtong Wang,[1] Anne Hoffmann,[5] Vincent Gardeux,[6,7] Bart Deplancke,[6,7] Laith Abu-Nawwas,[6,7] Patrik Stefanicka,[8,9] Lukas Varga,[8,10] Jonatan R. Ruiz,[11,12,13] Matthias Blüher,[5,14] Miroslav Balaz,[10,15] Anand Kumar Sharma,[16,*] and Christian Wolfrum[1,17,18,*]

[1]Laboratory of Translational Nutrition Biology, Institute of Food Nutrition and Health, Department of Health Sciences and Technology, ETH Zurich, Schwerzenbach, Switzerland
[2]Laboratory of Organic Chemistry, Department of Chemistry and Applied Biosciences, ETH Zurich, Zurich, Switzerland
[3]Department of Bioengineering, Stanford University, Stanford, CA, USA
[4]Stem Cell Bio Regenerative Med Institute, Stanford University, Stanford, CA, USA
[5]Helmholtz Institute for Metabolic, Obesity and Vascular Research (HI-MAG) of the Helmholtz Zentrum München at the University of Leipzig and University Hospital Leipzig, Leipzig, Germany
[6]Laboratory of Systems Biology and Genetics, Institute of Bioengineering, School of Life Sciences, Ecole Polytechnique Fédérale de Lausanne (EPFL), Lausanne, Switzerland
[7]Swiss Institute of Bioinformatics, Lausanne, Switzerland
[8]Department of Otorhinolaryngology-Head and Neck Surgery, Faculty of Medicine and University Hospital, Comenius University in Bratislava, Bratislava, Slovakia
[9]Department of Otorhinolaryngology - Head and Neck Surgery, Bory Hospital, Bratislava, Slovakia
[10]Biomedical Research Center, Slovak Academy of Sciences, Bratislava, Slovakia
[11]Department of Physical Education and Sports, Faculty of Sport Sciences, Sport and Health University Research Institute (iMUDS), University of Granada, Granada, Spain
[12]Centro de Investigación Biomédica en Red Fisiopatología de la Obesidad y Nutrición (CIBERobn), Instituto de Salud Carlos III, Madrid, Spain
[13]Instituto de Investigación Biosanitaria, ibs.Granada, Granada, Spain
[14]Department of Endocrinology, Nephrology, Rheumatology, University Hospital Leipzig, Leipzig, Germany
[15]Department of Animal Physiology and Ethology, Faculty of Natural Sciences, Comenius University in Bratislava, Bratislava, Slovakia
[16]Adaptive Metabolism Laboratory, Department of Metabolism, Digestion and Reproduction, Imperial College London, London, UK
[17]Nanyang Technological University (NTU), 50 Nanyang Avenue, Singapore, Singapore
[18]Lead contact
*Correspondence: a.sharma2@imperial.ac.uk (A.K.S.), christian.wolfrum@ntu.edu.sg (C.W.)
https://doi.org/10.1016/j.molcel.2026.02.001

SUMMARY

Induction of catabolic adipocyte activity independent of mitochondrial uncoupling to induce energy expenditure has received increasing attention. In this study, we identified mesenteric estrogen-dependent adipogenesis gene (*MEDAG*), a poorly studied gene, as a promising therapeutic target for enhancing energy expenditure in adipocytes. We demonstrated that adipose *MEDAG* expression positively correlates with obesity and metabolic dysfunction in humans. Consistently, adipocyte-specific ablation of *Medag* in mice leads to increased energy expenditure, offering protection from diet-induced obesity. Mechanistically, we show that MEDAG functions as an A-kinase-anchoring protein (AKAP), which can directly regulate protein kinase A (PKA) activity through a negative feedback loop, involving direct interaction with PKA leading to MEDAG phosphorylation and consequent feedback fine-tuning of PKA activity. Specifically, the direct interaction of MEDAG with the PKA-RIIβ subunit regulates the stability of PKA-RIIβ to prevent PKA hyperactivation. These findings position MEDAG as a target for adipose energy expenditure and uncover its AKAP activity.

INTRODUCTION

Obesity and related metabolic disorders have reached epidemic proportions globally. Although recent years have seen a development of highly efficacious anti-obesity therapeutics, the heterogeneity in etiology and responsiveness to pharmacological treatments necessitates a deeper understanding of energy homeostasis and the mechanisms regulating energy balance.[1] Energy homeostasis, i.e., the equilibrium between energy intake and expenditure, is crucial for maintaining metabolic health.

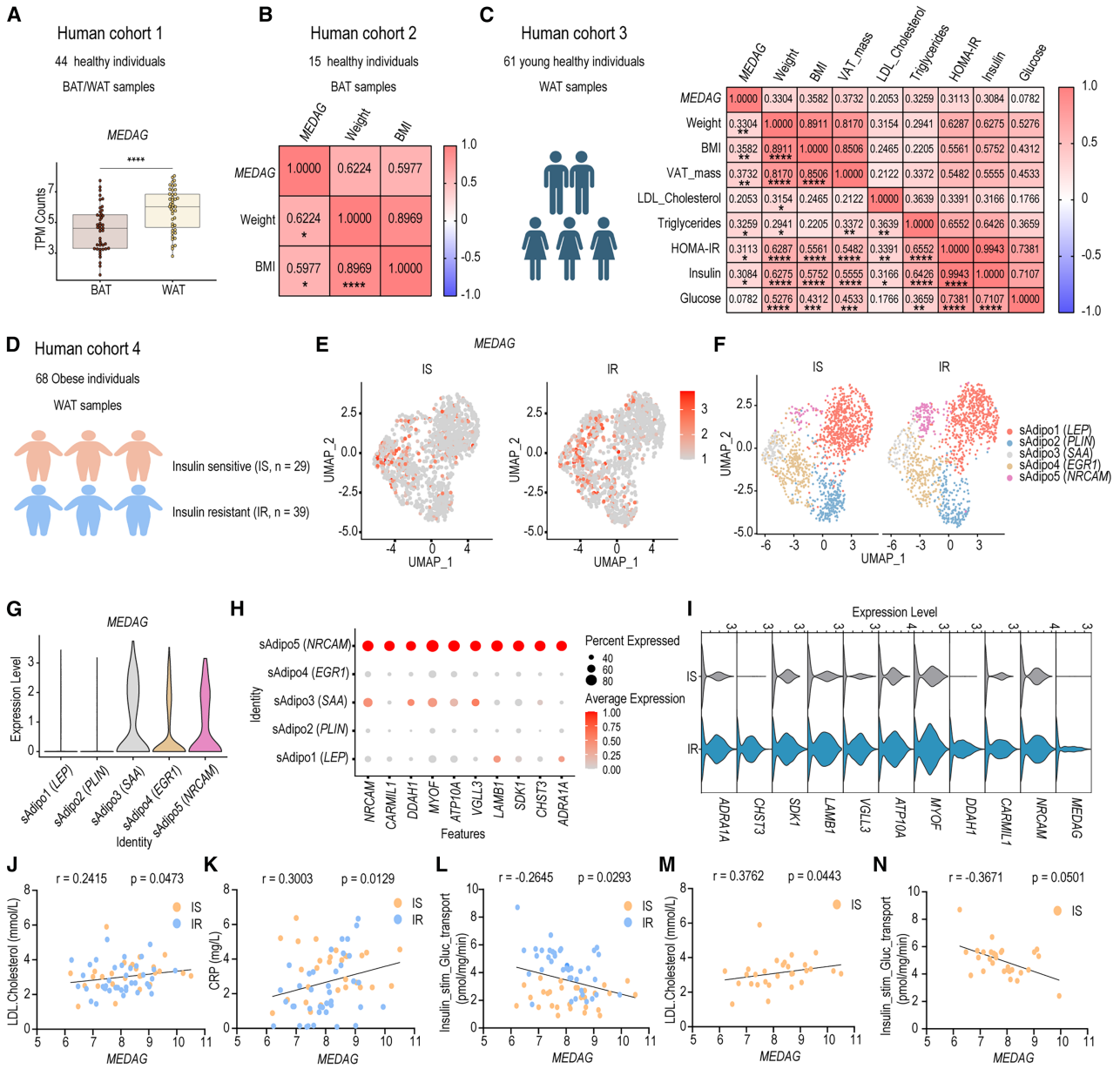

Figure 1. Adipose tissue *MEDAG* expression positively correlates with obesity and metabolic dysfunction in humans

(A) *MEDAG* expression in paired BAT and WAT from human cohort 2 consisting of 44 healthy individuals with bulk RNA-seq of paired BAT and WAT (n = 44).

(B) Correlation between supraclavicular BAT *MEDAG* expression and clinical parameters in human cohort 1 (n = 15 healthy individuals).

(C) Correlation between subcutaneous WAT *MEDAG* expression and clinical parameters in human cohort 3 (n = 61 healthy individuals).

(D) Human cohort 4 consisting of 68 individuals with obesity with subcutaneous WAT analysis (29 insulin sensitive and 39 insulin resistant).

(E) Feature plots showing *MEDAG* expression in the subcutaneous adipocytes from snRNA-seq analysis in human cohort 4.

(F) Uniform manifold approximation and projection (UMAP) plots showing different subcutaneous adipocyte subpopulations from the integrated analysis of snRNA-seq analysis in human cohort 4.

(G) Violin plots showing *MEDAG* expression in subcutaneous adipocyte subpopulations in human cohort 4.

(H) Dot plots displaying the top ten markers within the *NRCAM*+ subpopulation of subcutaneous adipocytes in human cohort 4.

(I) Violin plots comparing *MEDAG* expression and the top ten markers of the *NRCAM*+ subpopulation between metabolically healthy (IS) vs. unhealthy (IR) human subcutaneous WAT in human cohort 4.

(J–L) Correlation of subcutaneous WAT *MEDAG* expression with plasma LDL cholesterol levels (J), CRP, K), and insulin-stimulated glucose transport (L) in human cohort 4.

(legend continued on next page)

CellPress
OPEN ACCESS

Disruption of this balance by a chronic energy surplus state is an established underlying factor in obesity and metabolic disorders.[2] Therefore, discerning the energy-expending mechanisms is of basic and therapeutic interest.

Brown adipose tissue (BAT) activation contributes to metabolic health by acting as a metabolic sink and secreting BATokines.[3–5] Brown adipocytes are specialized energy-expending cells with high mitochondrial density[6] and uncoupling protein-1 (UCP-1) expression.[7] White adipocytes perform lipid storage and endocrine function and can also interconvert into *UCP-1*$^+$ beige adipocytes.[8] While quantitatively limited, many adult humans also have detectable BAT with a higher prevalence in those living in colder climates.[9] The presence of active BAT is associated with a lower body mass index (BMI) and improved cardiovascular health.[10–12] Consistently, the detectability of catabolic brown and beige adipocytes is negatively correlated with metabolic dysfunction,[12–14] highlighting their potential in tackling cardiometabolic health challenges.[15] However, a detailed mechanistic understanding of positive and negative regulatory pathways is a prerequisite for therapeutic prospects. In this regard, protein kinase A (PKA) is an attractive target amenable to pharmacological modulation. It is a crucial regulator of metabolism and energy balance by functioning as a versatile kinase for multiple proteins in the energy mobilization pathway.[16] Some human studies suggested an adipose-specific impairment of PKA in obesity.[17] Moreover, some Food and Drug Administration (FDA)-approved anti-obesity drugs, including glucagon-like peptide -1 (GLP-1) receptor agonists, utilize cyclic AMP (cAMP)/PKA signaling pathways to promote weight loss by enhancing lipolysis, reducing appetite, and improving insulin sensitivity.[18] These findings underscore the potential therapeutic relevance of targeting cAMP/PKA signaling in obesity management and metabolic health interventions.

The active PKA holoenzyme is a tetramer composed of two regulatory (PKA-R) and two catalytic subunits (PKA-C) with several specialized tissue-specific subunit isoforms.[19] Adipose tissue predominantly expresses PKA-RIIβ.[20] In the absence of PKA-RIIβ, adipocytes switch to PKA-RIα, which enhances basal PKA activity and UCP-1 expression.[21] Besides subunit constitution, the cAMP binding to regulatory subunits directly modulates PKA activity.[22] cAMP levels are regulated through adenylate cyclase (synthesis) and phosphodiesterase (degradation).[23] Besides, A-kinase-anchoring proteins (AKAPs) regulate the spatiotemporal localization of PKA via a direct interaction to facilitate subcellular compartmentalization-mediated modulation of PKA activity.[24] However, adipocyte-specific PKA regulation remains poorly characterized.[25] Given the profound regulatory effect of AKAPs, the identification of adipocyte-specific AKAPs and the modulation of PKA-AKAP interactions present a potential strategy to modulate energy expenditure.

In this study, we uncovered the AKAP activity of the mesenteric estrogen-dependent adipogenesis gene (MEDAG). The earliest discovery implicated visceral adipose tissue *MEDAG* expression in female hormonal imbalances and suggested its pro-adipogenic role.[26] We found that adipose *MEDAG* expression correlates with obesity and metabolic disorders. We confirmed the inhibitory role of *MEDAG* in adipocyte respiration and demonstrated that ablation of *Medag* in adipocytes enhances energy expenditure, counteracts obesity, and increases glucose utilization in an insulin-independent manner. Mechanistically, these effects are driven by the identified AKAP activity of MEDAG that directly modulates PKA activity in adipocytes.

RESULTS

Adipose tissue *MEDAG* expression positively correlates with obesity and metabolic dysfunction in humans

Considering the therapeutic potential of catabolic adipocytes activation, we aimed to discover candidate proteins that can be targeted to increase the functionality of these specific adipocytes. We first analyzed the transcriptome of human BAT and white adipose tissue (WAT) to identify genes differentially expressed between paired human deep neck BAT and subcutaneous WAT biopsies. We also emphasized gene conservation across species as a proxy of functional essentiality and translatability.

We noted that *MEDAG* was highly enriched in WAT compared with BAT in a human cohort (cohort 1) comprising paired BAT/WAT samples from 44 healthy individuals (32 female, 12 male, age = 45.68 ± 16 years, BMI = 25.52 ± 4.15 kg/m^2) (Figure 1A). In a previously published dataset[27] (cohort 2) that included BAT gene expression and paired clinical parameters from 15 healthy male individuals (age = 25.45 ± 4.68 years, BMI = 22.5 ± 2.4 kg/m^2) to study effect of glucocorticoid treatment on BAT activity, we observed a strong positive correlation between BAT *MEDAG* expression and body weight as well as BMI (Figure 1B). To further gauge the physiological relevance of WAT *MEDAG* in humans, we analyzed the WAT gene expression data together with paired clinical parameters from an additional independent cohort (cohort 3) of 61 healthy individuals (48 female, 13 male, age = 22.27 ± 2.03 years, BMI = 25.7 ± 4.53 kg/m^2) from the Activating Brown Adipose Tissue Through Exercise (ACTIBATE) cohort.[28] The WAT *MEDAG* expression showed a positive correlation with unhealthy anthropometric traits such as body weight, BMI, visceral adipose tissue mass, triglycerides (TGs), plasma insulin levels, and HOMA-IR (homeostasis model assessment of insulin resistance) (Figure 1C). Collectively, these findings suggest a general association of adipose *MEDAG* with obesity.

In a previously published subcohort (cohort 4) from the Leipzig Obesity BioBank, consisting of 68 individuals with obesity (29 insulin sensitive, 39 insulin resistant) (Figure 1D), *MEDAG* was specifically associated with metabolic dysfunction based on the single-nuclei RNA sequencing (snRNA-seq) of subcutaneous white adipocytes (Figure 1E). In this study, out of the five identified adipocyte subpopulations in subWAT

(M and N) Correlation of subcutaneous WAT *MEDAG* expression with plasma LDL cholesterol levels (M) and insulin-stimulated glucose transport (N) in the subset of metabolically healthy individuals (n = 29).

Statistical significance was calculated using DeSeq2 (A), Pearson correlation coefficients (B and C), and Spearman correlation coefficients (J–N). ns, not significant, *$p < 0.05$, **$p < 0.01$, ****$p < 0.0001$.

See also Figure S1.

(Figure 1F), *MEDAG* was highly expressed in *SAA*$^+$, *EGR1*$^+$, and *NRCAM*$^+$ subpopulations (Figure 1G). Reference mapping against the human adipocyte atlas by Emont et al.[29] predicted that most of the subpopulations correspond to basal adipocytes.[30] The *EGR1*$^+$ subpopulation shared a gene expression signature with the hAd1 subpopulation. In contrast, the *SAA*$^+$ and *NRCAM*$^+$ subpopulations exhibited signatures of the hAd4 subpopulation, with the enrichment of unsaturated fatty acid synthesis pathways. We also validated the expression of established hAd1 and hAd4 marker genes within five adipocyte subpopulations to confirm their conserved functional identities (Figure S1A). Importantly, *MEDAG* expression in the Emont et al. dataset[29] was highest in hAd1 and hAd4 subpopulations (Figure S1B), with upregulated expression in individuals with a BMI range of 40–50 (Figure S1C), reinforcing its obesity-associated expression pattern across independent cohorts. The *NRCAM*$^+$ subpopulation was particularly prevalent in individuals with IR (Figure 1F). *NRCAM* expression correlates with plasma LDL cholesterol levels and is part of an obesity-related transcriptional network.[29,31] Moreover, the top ten markers within the *NRCAM*$^+$ subpopulations were highly expressed in insulin-resistant individuals (Figures 1H and 1I). Similarly, top markers of hAd1 and hAd4 showed a strong positive correlation with LDL cholesterol[29] with higher expression in insulin-resistant individuals (Figure S1D). Thus, the enrichment of *MEDAG* in the *NRCAM*$^+$ subcutaneous adipocyte subpopulation may reflect a link to cardiovascular risk and dyslipidemia (Figure 1I).

Additionally, analysis of bulk RNA-seq data from the same cohort revealed that WAT *MEDAG* expression is positively correlated with plasma LDL cholesterol levels and C-reactive protein (CRP), while showing a negative correlation with insulin-stimulated glucose transport (Figures 1J–1L). These correlations with LDL cholesterol and insulin-stimulated glucose transport were more pronounced among insulin-sensitive individuals with obesity, indicating the plausible regulatory involvement of *MEDAG* in broader adipose tissue metabolic pathophysiology (Figures 1M and 1N).

These findings link adipose *MEDAG* expression to obesity and metabolic dysfunctions and highlight its potential as a therapeutic target. Despite the striking enrichment profile and promising association with obesity, pointing toward potential functional specialization, adipose-specific functions of *MEDAG* are unexplored. We, therefore, selected *MEDAG* for a detailed study.

Medag regulates adipocyte respiration by PKA activity modulation

To discern the mechanistic underpinnings of *MEDAG*-mediated adipose metabolic regulation, we used mouse cell/animal model systems. We first validated that the respiratory effect of *Medag* knockdown (KD) in mouse catabolic adipocytes (immortalized brown adipocytes [iBAs]) (Figures 2A and 2B). *Medag* KD also increased glycolytic flux with unaltered glycolytic capacity (Figures 2C and 2D). Moreover, given the effect of *Medag* KD on isoproterenol-stimulated oxygen consumption, we investigated its effect on lipolysis. *Medag* KD increased isoproterenol-stimulated, but not basal lipolysis with increased glycerol and free fatty acid release (Figures 2E and 2F), with a cell-state-dependent modulation of substrate utilization. Under basal conditions, *Medag* KD preferentially increased glucose oxidation. Following isoproterenol stimulation, however, KD cells exhibited comprehensive enhancement of fatty acid, glucose, and glutamine oxidation (Figures S2A and S2B).

To define the underlying signaling cascade involved in *Medag* functioning, we analyzed the expression/modification of key proteins involved in lipolysis, glucose/insulin signaling, and thermogenesis pathways. While markers of glucose/insulin signaling were unperturbed, phosphorylated HSL hormone-sensitive lipase (P-HSL) and phosphorylated cAMP-responsive element-binding protein (P-CREB) levels were significantly elevated in *Medag* KD at early (1 h) and late (12 h) time points after isoproterenol stimulation (Figure S2C). Since P-HSL and P-CREB are bona fide PKA targets in adipocytes, it prompted us to investigate the direct involvement of PKA. Consistently, *Medag* KD enhanced PKA activity at basal and isoproterenol-stimulated states, despite unchanged cAMP levels (Figures 2G and 2H). Direct PKA activity assays confirmed elevated PKA activity in *Medag* KD adipocytes (Figure 2I). Interestingly, PKA was mainly localized in the cytoplasm at the basal state, and isoproterenol stimulation triggered its nuclear translocation (Figure 2J). This spatial partitioning allows PKA to concurrently regulate cytoplasmic and nuclear substrates. The cytoplasmic activity, marked by increased P-HSL levels, underscores PKA's role in regulating cytoplasmic processes. In contrast, nuclear PKA activation is reflected in P-CREB levels and mediates transcriptional responses to adrenergic signals to enhance thermogenic capacity (Figure 2K). Nuclear translocation is a well-documented feature of PKA, enabling compartmentalized regulation of rapid (e.g., lipolysis) vs. delayed (e.g., gene expression) responses to β-adrenergic stimuli.[32,33] However, there were no significant changes in the transcriptional levels of established thermogenic markers (Figure S2D), plausibly because of saturating activation of peroxisome proliferator-activated receptor gamma (PPARγ) signaling by rosiglitazone (present in the differentiation cocktail). Notably, overexpression (OE) of MEDAG did not alter PKA activity at basal or isoproterenol-stimulated states (Figure S2E). Nevertheless, isoproterenol-stimulated respiration and maximal respiration capacity of *Medag* KD cells were attenuated by PKA inhibitor (H89), underscoring the essential role of PKA (Figures 2L–2N). Similarly, H89 diminished the P-HSL and P-CREB induction in *Medag* KD (Figure 2O), suggesting that PKA activation mediates the increased mitochondrial respiration in *Medag*-deficient brown adipocytes.

We next assessed conservation of MEDAG-mediated PKA regulation in white adipocytes. *Medag* KD elevated basal PKA activity but did not alter isoproterenol-stimulated responses (Figure S2F). Given this phenotypic divergence, we quantified *Medag* expression dynamics. In brown adipocytes, acute isoproterenol exposure did not alter *Medag* mRNA expression (Figure S2G), while prolonged stimulation dramatically induced it (Figure S2D). Conversely, white adipocytes exhibited reduced *Medag* mRNA following isoproterenol stimulation (Figure S2H). This cell-type-specific transcriptional regulation likely underlies the diminished phenotypic impact of *Medag* KD in white adipocytes under stimulated conditions.

CellPress
OPEN ACCESS

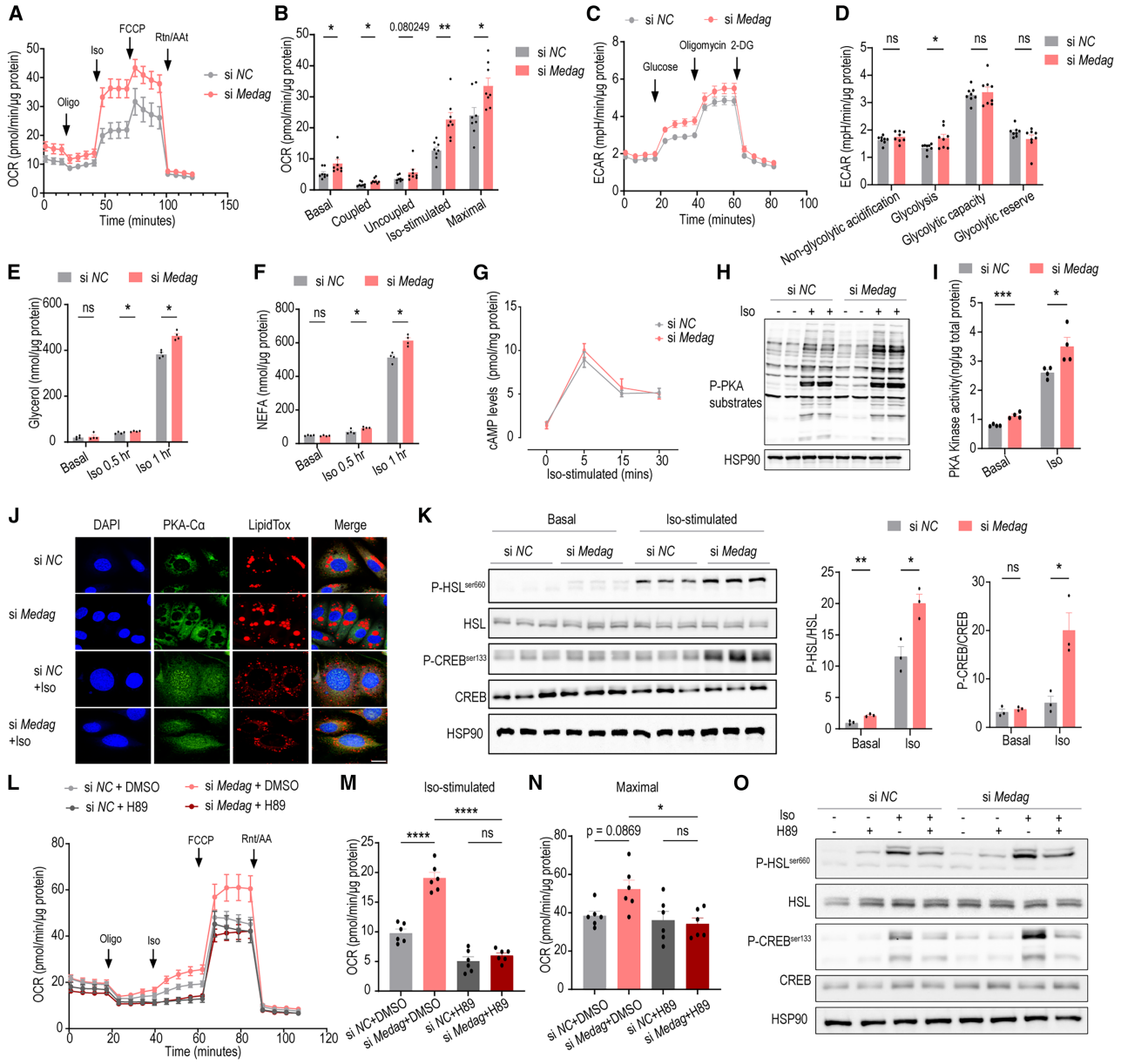

Figure 2. *Medag* regulates adipocyte respiration by PKA activity modulation

(A and B) Oxygen consumption rate (A) and quantification (B) in iBAs transfected with control siRNA (si NC) or siRNA against *Medag* (n = 8).

(C and D) Extracellular acidification rate (ECAR) curve (C) and calculation (D) in iBAs transfected with control siRNA (si NC) or siRNA against *Medag* (n = 8).

(E and F) Glycerol (E) and non-esterified fatty acid (NEFA) (F) concentration in the medium of iBAs treated with 1 μM isoproterenol for 0.5 or 1 h after *Medag* knockdown (n = 4).

(G) cAMP levels in iBAs after 1 μM isoproterenol stimulation at different time points following *Medag* knockdown (n = 3).

(H) Representative blots of p-PKA substrates levels in iBAs treated with 1 μM isoproterenol for 1 h after *Medag* knockdown (n = 2).

(I) PKA kinase activity of in iBAs treated with 1 μM isoproterenol for 1 h after *Medag* knockdown (n = 4).

(J) Immunostaining with PKA-Cα in iBAs treated with 1 μM isoproterenol for 1 h after *Medag* knockdown (scale bar, 100 μm).

(K) Representative blots and quantification of P-HSL and P-CREB protein levels in iBAs treated with 1 μM isoproterenol for 0.5 h after *Medag* knockdown (n = 3).

(L–N) Oxygen consumption curve (L), calculation of isoproterenol stimulated (M), and maximal oxygen consumption (N) in iBAs pre-treated with 10 μM PKA inhibitor H89 for 1 h after *Medag* knockdown (n = 6).

(O) Representative blots of P-HSL and P-CREB protein levels in iBAs treated with 1 μM isoproterenol for 1 h following pre-treatment with 10 μM H89 for 1 h after *Medag* knockdown.

Data are presented as mean ± SEM and analyzed using unpaired two-tailed t test (B, D, and E–I) and two-way ANOVA with Tukey's post hoc multiple comparison test (M and N). ns, not significant, *$p < 0.05$, **$p < 0.01$, ****$p < 0.0001$.

See also Figure S2.

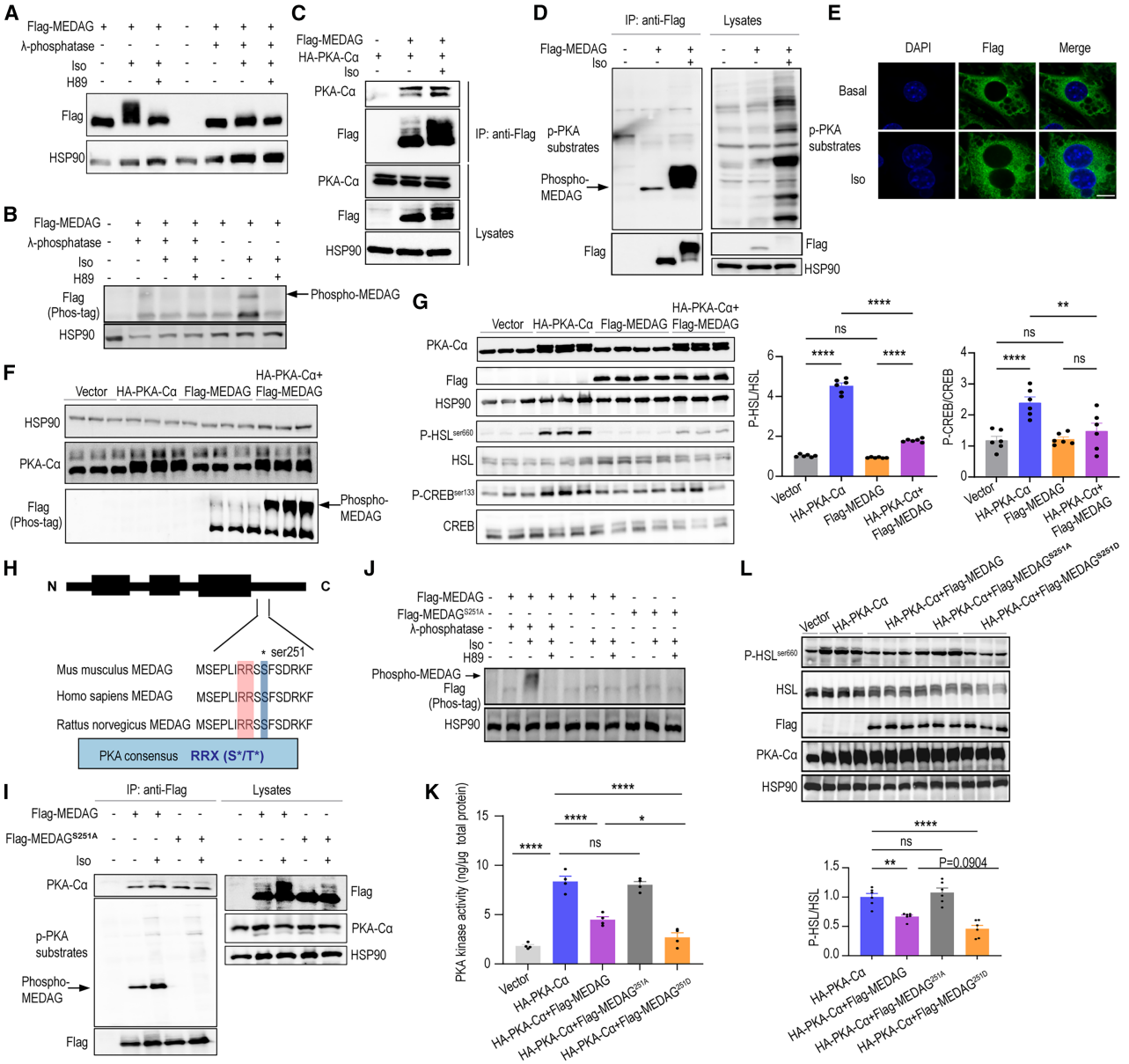

Figure 3. PKA and MEDAG form an autoregulatory loop

(A) Representative blots of MEDAG in iBAs expressing FLAG-MEDAG after pre-treatment with 10 μM H89 for 1 h, followed by 1 μM isoproterenol stimulation for 1 h. The total cell lysates were treated with λ-phosphatase.

(B) Phospho-specific mobility shift assay resolved by Phos-tag SDS-PAGE. Blots probed with anti-FLAG antibody. λ-phosphatase-treated samples confirm shift specificity.

(C) iBAs co-expressing FLAG-MEDAG and hemagglutinin (HA)-PKA-Cα were treated with 1 μM isoproterenol for 1 h. The total cell lysates were subjected to IP against FLAG, followed by immunoblotting.

(D) iBAs expressing FLAG-MEDAG were treated with 1 μM isoproterenol for 1 h. The total cell lysates were subjected to IP against FLAG, followed by immunoblotting.

(E) Immunofluorescence of MEDAG in iBAs expressing FLAG-MEDAG treated with 1 μM isoproterenol for 1 h (scale bar, 10 μm).

(F) Phos-tag SDS-PAGE analysis of FLAG-MEDAG phosphorylation in iBAs expressing FLAG-MEDAG, HA-PKA-Cα, or both (n = 3).

(G) Representative blots and quantification of P-HSL and P-CREB protein levels in iBAs expressing FLAG-MEDAG, HA-PKA-Cα, or both (n = 6).

(H) Identification of the PKA consensus motif within MEDAG protein across different species.

(I) iBAs expressing WT-MEDAG or S251A-MEDAG were treated with 1 μM isoproterenol for 1 h. The total cell lysates were subjected to IP against FLAG, followed by immunoblotting.

(J) Phos-tag SDS-PAGE analysis of FLAG-MEDAG phosphorylation in iBAs expressing FLAG-MEDAG or phosphorylation-deficient S251A mutant.

(K) PKA kinase activity in iBAs expressing WT-MEDAG, S251A-MEDAG, S251D-MEDAG, PKA-Cα, or combinations thereof (n = 4).

(legend continued on next page)

CellPress
OPEN ACCESS

Collectively, these data establish MEDAG as a fundamental regulator of adipocyte respiration through PKA-dependent signaling mechanisms.

PKA and MEDAG form an autoregulatory loop

Having established the molecular players of *Medag* KD-driven respiration, we sought to investigate the mechanism of PKA regulation by MEDAG. To examine the temporal correlations of PKA activation and MEDAG expression, we designed a MEDAG OE system in iBAs. Given the absence of validated MEDAG-specific antibodies, we generated a FLAG-tagged MEDAG construct (FLAG-MEDAG) to enable detection. Validation experiments confirmed robust FLAG-MEDAG expression at the expected molecular weight. Crucially, small interfering RNA (siRNA) targeting *Medag* effectively reduced FLAG-MEDAG signal by >80%, demonstrating both construct specificity and efficient target depletion across experiments (Figure S2I).

Interestingly, isoproterenol stimulation triggered a mobility shift in MEDAG, invoking the possibility of post-translational modification (Figure 3A). Since the distance shift was rather slight, we reckoned a smaller modification moiety. The phosphatase treatment confirmed that the shift was due to phosphorylation. Notably, the mobility shift disappeared when cells were treated with H89, suggesting that MEDAG might be a direct phosphorylation target of PKA (Figure 3A). To resolve phosphorylation dynamics with higher sensitivity, we employed Phos-tag SDS-PAGE. This revealed a mobility shift in MEDAG following isoproterenol stimulation, which was reversed by H89 pretreatment or phosphatase treatment, confirming PKA-dependent MEDAG phosphorylation (Figure 3B). With co-immunoprecipitation (coIP) analysis, we confirmed that MEDAG binds to PKA-Cα at both basal states and after isoproterenol stimulation, with enhanced phosphorylation observed under stimulated conditions (Figure 3C). The p-PKA substrates immunoblotting of the FLAG-MEDAG immunoprecipitated proteins further supported that PKA phosphorylates MEDAG (Figure 3D). The immunostaining suggested that MEDAG is confined to the cytoplasm, ruling out the co-translocation of MEDAG to the nucleus with PKA (Figures 2J and 3E). When we overexpressed the catalytic PKA-Cα subunit in iBAs, it induced the characteristic phosphorylation-dependent mobility shift in MEDAG (Figure 3F). Notably, PKA-Cα OE elevated PKA activity (measured by P-HSL and P-CREB levels), and this hyperactivation was attenuated by MEDAG co-expression (Figure 3G). In contrast, MEDAG OE alone did not suppress the basal PKA activity (Figures 3G and S2E), suggesting that MEDAG fine-tunes the PKA activity to preclude excessive activation in a yet unknown stoichiometric fashion.

We next investigated the PKA phosphorylation site in MEDAG. We noted a conserved PKA consensus motif at serine 251 in MEDAG (Figure 3H). Substituting serine with alanine (S251A) abolished the MEDAG phosphorylation in basal and isoproterenol-stimulated states without affecting the PKA-Cα binding (Figure 3I), confirming that PKA phosphorylates MEDAG at Ser251. This was further validated by Phos-tag analysis, showing complete loss of phosphorylation-dependent mobility shift in the S251A mutant (Figure 3J). To functionally characterize phospho-MEDAG, we generated a phospho-mimetic mutant (S251D). OE of S251D significantly reduced the PKA and diminished HSL phosphorylation (Figure 3L). Conversely, the phosphorylation-deficient S251A mutant showed no suppressive activity (Figure 3L). These findings confirm that S251 phosphorylation serves as the molecular switch activating MEDAG's regulatory capacity. Notably, wild-type (WT) MEDAG OE alone failed to alter PKA signaling outputs (Figure S2E), likely due to insufficient phosphorylation under these conditions, where the low phospho-MEDAG to total MEDAG ratio prevents functional inhibition.

These results demonstrate that S251 phosphorylation of MEDAG by PKA is vital for negative feedback to PKA.

MEDAG regulates the stability of the PKA-RIIβ subunits

Based on the observed regulation of PKA activity by MEDAG, we next examined the molecular details of this regulation. PKA is a heterotetrameric kinase with two regulatory and two catalytic subunits. In the absence of cAMP, the regulatory subunits inhibit the catalytic subunits. cAMP binding at two sites on each regulatory subunit relieves the inhibitory effects on the kinase activity. In adipose tissue, PKA-RIIβ pairing with Cα is the predominant configuration of PKA holoenzyme.[17] We noted a peculiar reduction in PKA-RIIβ, but not PKA-RIα, levels in *Medag* KD at basal levels, which became more pronounced at isoproterenol-stimulated state (Figure 4A). This change was not due to decreased translation, as mRNA levels remained largely unaffected (Figure S3A). Instead, we observed higher K48-linked ubiquitination of PKA-RIIβ in *Medag*-deficient adipocytes (Figure 4B). K48-linked polyubiquitin chains specifically target substrates for proteasomal degradation, distinguishing them from K63-linked chains that typically mediate non-proteolytic signaling functions.[34] This finding establishes that MEDAG deficiency primarily promotes PKA-RIIβ degradation via the ubiquitin-proteasome pathway. This regulatory mechanism was conserved across adipocyte models. *Medag*-deficient white adipocytes exhibited reduced basal PKA-RIIβ expression along with elevated PKA activity (Figures S2F and S3B).

We next explored whether the physical interaction of MEDAG with PKA-RIIβ influences its stability. In brown adipocytes, MEDAG and PKA-RIIβ spatially co-localize at both basal and isoproterenol stimulation (Figure 4C). In addition, both WT and mutant MEDAG could bind to PKA-RIIβ. However, isoproterenol stimulation led to the dissociation of the complex (Figure 4D), possibly due to decreased PKA-RIIβ expression or a conformational change in the complex caused by cAMP binding. The S251A mutant MEDAG, which cannot be phosphorylated, showed a stronger association with PKA-RIIβ, indicating that phosphorylation may alter MEDAG's association with PKA-RIIβ and influence PKA activity indirectly by modulating subunit

(L) Representative blots and quantification of P-HSL protein levels in iBAs expressing WT-MEDAG, S251A-MEDAG, S251D-MEDAG, PKA-Cα, or combinations thereof (n = 6).

Data are presented as mean ± SEM and analyzed using two-way ANOVA with Tukey's post hoc multiple comparison test (G, K, and L). ns, not significant, $^{**}p < 0.01$, $^{****}p < 0.0001$.

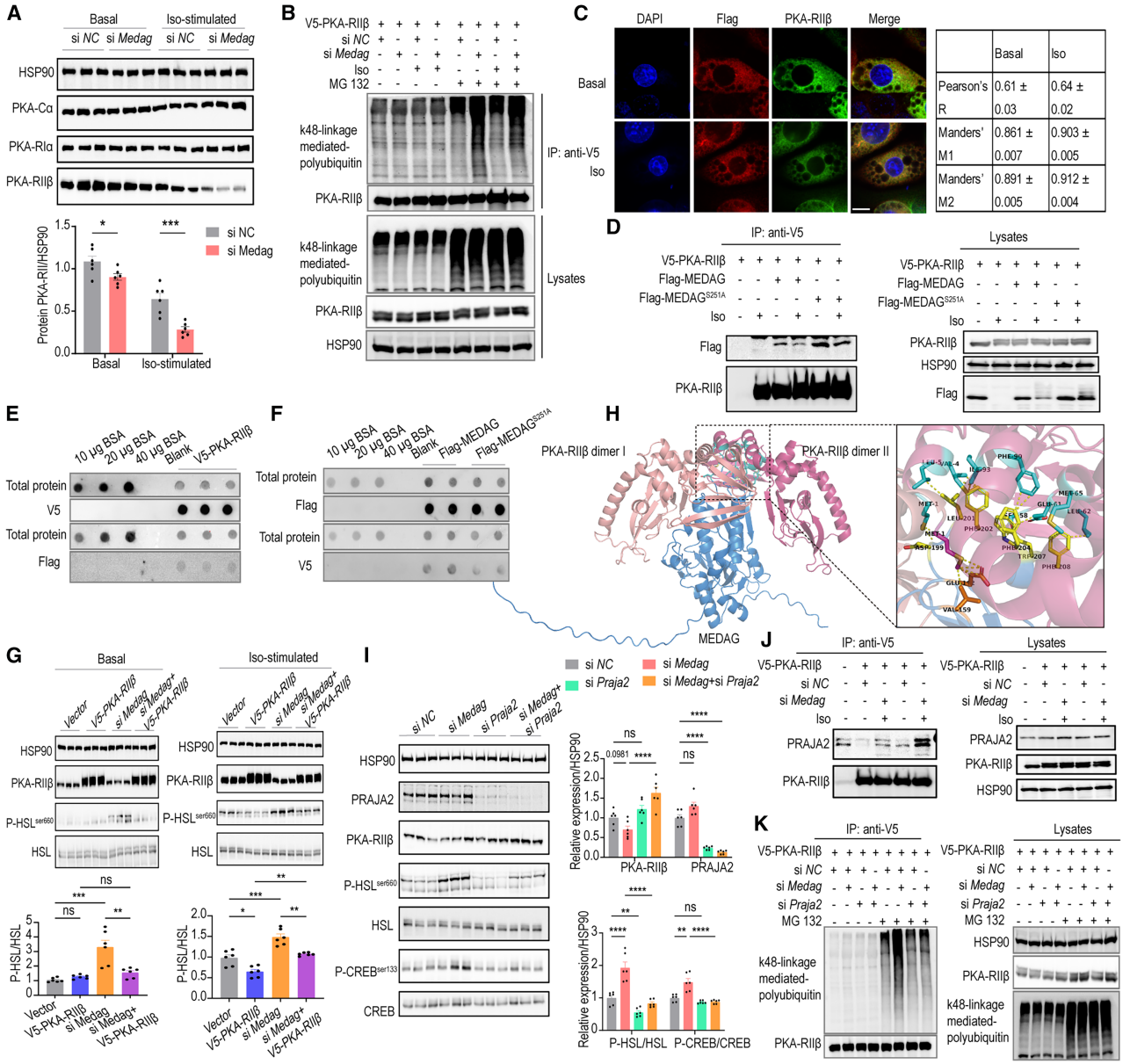

Figure 4. MEDAG regulates the stability of the PKA-RIIβ subunits

(A) Representative blots and quantification of PKA-RIIβ protein levels in iBAs under basal conditions and following isoproterenol stimulation after *Medag* knockdown ($n = 6$).

(B) Detection of K48-linkage polyubiquitylation patterns in iBAs expressing V5-PKA-RII at basal states and after isoproterenol stimulation states following *Medag* knockdown.

(C) Representative confocal microscopy images (left) and quantification (right) of FLAG-MEDAG (red) and PKA-RIIβ (green) co-localization in iBAs expressing FLAG-MEDAG. Cells were treated with 1 μM isoproterenol or vehicle for 1 h. Scale bar, 10 μm. Co-localization was quantified using Coloc2 plugin in Fiji/ImageJ ($n = 20$ cells).

(D) iBAs co-expressing V5-PKA-RII with either WT-MEDAG or S251A-MEDAG were treated with isoproterenol. The total cell lysates were subjected to IP against V5, followed by immunoblotting.

(E) Direct binding assay using immunoaffinity-captured proteins. Recombinant V5-PKA-RIIβ (bait; immunoaffinity-captured via anti-V5 resin) was spotted onto nitrocellulose membrane, overlaid with recombinant FLAG-MEDAG (probe; immunoaffinity-captured via anti-FLAG resin), and detected with anti-FLAG antibody. Total spotted protein was visualized by Ponceau S staining.

(F) Recombinant FLAG-MEDAG (WT) and phosphorylation-deficient mutant (S251A) (baits; immunoaffinity-captured via anti-FLAG resin) were spotted, overlaid with recombinant V5-PKA-RIIβ (probe; immunoaffinity-captured via anti-V5 resin), and detected with anti-V5 antibody. Total spotted protein was visualized by Ponceau S staining.

(legend continued on next page)

CellPress
OPEN ACCESS

accessibility and degradation. To determine whether this reflected direct binding or an indirect association with the complex, we employed protein overlay assays with purified immunoprecipitated proteins. This *in vitro* approach demonstrated robust direct binding between MEDAG and PKA-RIIβ (Figure 4E), with reciprocal validation of the interaction (Figure 4F). Strikingly, the S251A mutant showed a reduced binding affinity in this purified system. To further confirm the critical role of PKA-RIIβ expression in MEDAG-mediated change in PKA activity, we overexpressed PKA-RIIβ in iBAs. While this OE did not affect basal PKA activity, it significantly reduced PKA activity after isoproterenol stimulation, likely by enhancing the sequestration of PKA-Cα (Figure 4G). Additionally, PKA-RIIβ OE diminished the extent of the effect of *Medag* deficiency on P-HSL levels at both basal and stimulated states, highlighting that MEDAG modulates PKA activity through a direct PKA-RIIβ binding (Figure 4G). These findings suggested that MEDAG acts as an AKAP in adipocytes.

To gain further insights into the MEDAG-PKA-RIIβ complex, we performed structure modeling using AlphaFold 3 and identified several molecular interactions implicated in complex stabilization. MEDAG appears to stabilize two PKA-RIIβ monomers and may help in dimerization as it binds at the dimer interface. Met-1 from a PKA-RIIβ monomer interacts with MEDAG Val-159 and Glu-162 through hydrophobic interaction. Further, a hydrophobic core is formed between Val-4, Leu-5, and Ile-93 of the second PKA-RIIβ monomer and Leu-201 and Phe-202 of MEDAG. Additional hydrophobic interactions are established between Phe-90 from dimer II and Phe-204 from MEDAG, and Leu-62 and Met-65 from dimer II. Moreover, a hydrogen bond between the side chain of Ser-58 from dimer II and MEDAG Trp-207 is complemented by van der Waals interactions between the Trp-207 and Glu-61 from dimer II (Figures 4H and S3C). These strong interactions suggest that MEDAG binding to PKA-RIIβ will lead to a stable complex formation with relatively high binding affinity, which is validated by our experimental data. Intriguingly, simulations of phosphorylated MEDAG (pS251) revealed dramatic reorganization of the binding interface (Figure S3D), suggesting that phosphorylation triggers structural rearrangements that modulate complex stability. Collectively, the predicted structural complex and our functional data on MEDAG-PKA-RIIβ together demonstrate that MEDAG functions as an AKAP.

We next investigated the mechanisms of regulation of PKA-RIIβ abundance by MEDAG. E3 ubiquitin-protein ligase Praja-2 (PRAJA2) is a well-established E3 ligase known to ubiquitinate PKA-R subunits.[35] We, therefore, tested its role in adipocytes. *Praja2* KD abolished the decrease in PKA-RIIβ levels caused by *Medag* KD (Figure 4I). Importantly, *Praja2* KD alleviated *Medag*-KD-induced increase in cytoplasmic and nuclear PKA activity as indicated by the restored levels of P-HSL and P-CREB (Figure 4I). *Medag* KD did not alter PRAJA2 expression; it significantly enhanced the binding of PRAJA2 to PKA-RIIβ, particularly after isoproterenol stimulation (Figure 4J). Furthermore, *Medag* deficiency failed to enhance K48-linked ubiquitination of PKA-RIIβ when *Praja2* was depleted (Figure 4K). These findings suggest that MEDAG influences the stability of PKA-RIIβ through PRAJA2-mediated ubiquitination and subsequent proteasomal degradation.

These data demonstrate that MEDAG regulates PKA activity through direct binding to modulate PRAJA2-mediated ubiquitination and degradation. These functional and structural characteristics position MEDAG as a tentative AKAP in adipocytes.

Medag AKO mice exhibit increased energy expenditure and are resistant to HFD-induced obesity

To investigate the physiological relevance of adipose MEDAG, we generated adipocyte-specific *Medag* knockout (AKO) mice (Figure 5A). As expected, *Medag* mRNA expression was significantly downregulated in adipose tissue of AKO mice, confirming the knockout (KO) efficiency and validating the model (Figure S4A). On a high-fat diet (HFD), AKO mice displayed a remarkable reduction in body weight gain compared with WT controls. The reduction in body weight was primarily attributed to lower fat mass (Figures 5B–5D). Notably, unlike inguinal and epididymal adipose depots, interscapular BAT (iBAT) weight remained unaffected. Liver weight, as expected, was unchanged (Figure 5E). Furthermore, AKO mice showed lower plasma cholesterol and TG levels (Figures 5F and 5G). However, plasma fatty acid levels were unaltered (Figure S4B). Histological analyses showed that AKO mice have smaller adipocytes in epididymal WAT (eWAT) and inguinal WAT (iWAT) (Figure 5H). Despite these pronounced changes in adipose tissue organization, AKO mice showed minimal improvement in glucose tolerance and insulin sensitivity (Figures 5K–5N). Similarly, AKO mice showed a preserved rectal temperature (Figure S4C). Nevertheless, AKO mice showed lower fasting blood glucose levels (Figures 5K–5N), which is probably unrelated to insulin as suggested earlier.

We then evaluated the energy expenditure of AKO mice under thermoneutral (TN), room temperature (RT), and cold exposure

(G) Computational predicted structure complex of PKA-RIIβ dimer and MEDAG using AlphaFold 3. A closer look of the structural interface of the dimer and MEDAG is shown on the right. The residues from MEDAG involved in the interaction are shown in orange (interact with dimer I) and yellow (interact with dimer II).
(H) Representative blots and quantification of P-HSL in iBAs expressing V5-PKA-RII in combination with *Medag* knockdown under basal conditions and after isoproterenol stimulation ($n = 6$).
(I) Representative blots and quantification of PKA-RIIβ, P-HSL, P-CREB protein levels in iBAs after individual *Medag* knockdown, *Praja2* knockdown, or *Medag*/*Praja2* double knockdown ($n = 6$).
(J) iBAs expressing V5-PKA-RII in combination with *Medag* knockdown were treated with isoproterenol. The total cell lysates were subjected to IP against V5, followed by immunoblotting.
(K) Detection of K48-linkage polyubiquitylation patterns in iBAs expressing V5-PKA-RII at basal states and after isoproterenol stimulation states following *Medag* knockdown.
Data are presented as mean ± SEM and analyzed using unpaired two-tailed *t* test (A) and two-way ANOVA with Tukey's post hoc multiple comparison test (H and I). ns, not significant, $^{*}p < 0.05$, $^{**}p < 0.01$, $^{***}p < 0.001$, $^{****}p < 0.0001$.
See also Figure S3.

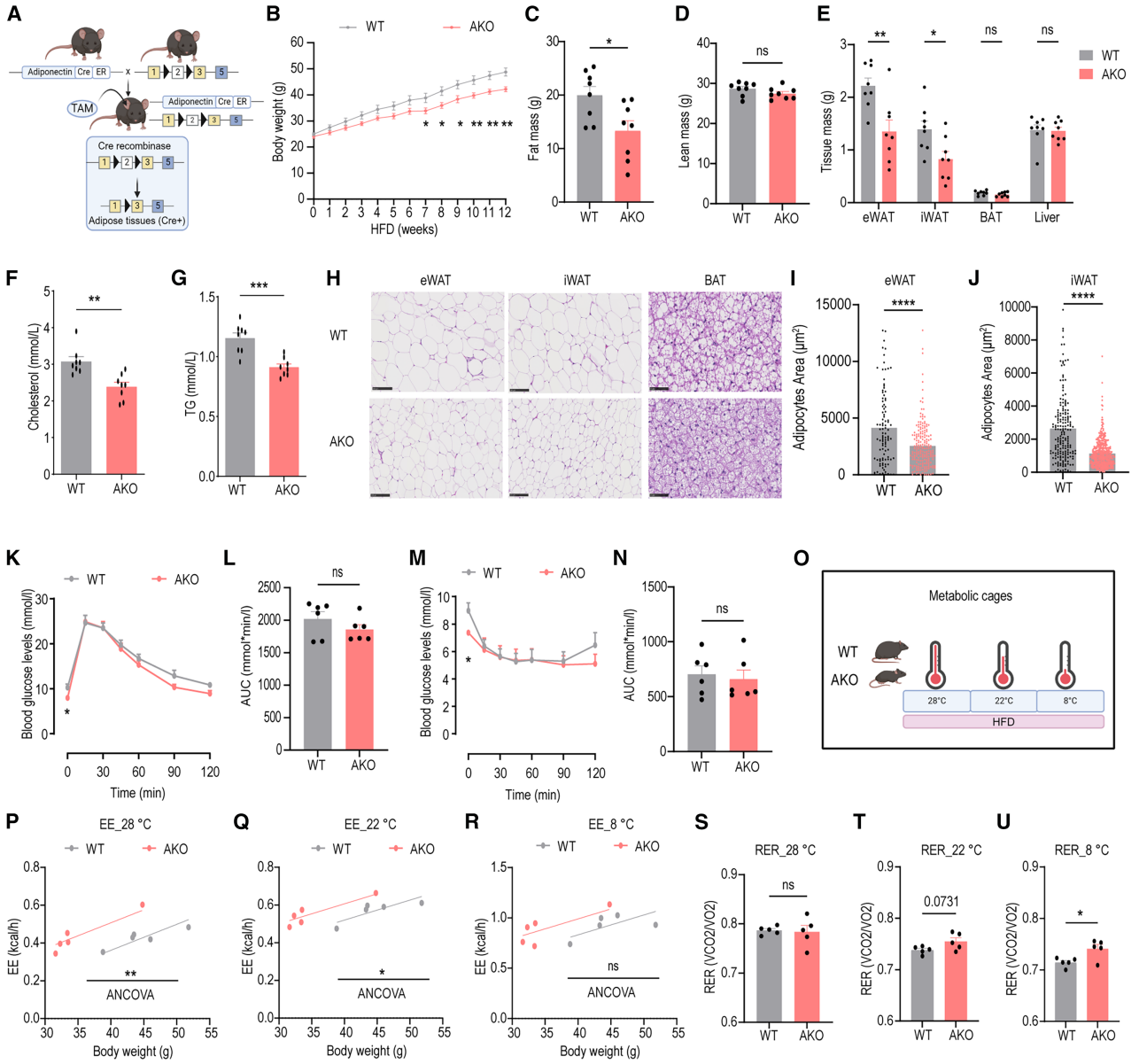

Figure 5. *Medag* AKO mice exhibit increased EE and are resistance to HFD-induced obesity

(A) Scheme of *Medag* AT KO mouse model.

(B) Body weight gain during 12 weeks of HFD feeding (n = 8).

(C) Fat mass after 12 weeks of HFD feeding (n = 8).

(D) Lean mass after 12 weeks of HFD feeding (n = 8).

(E) Mass of various adipose tissue depots and liver after 12 weeks of HFD feeding (n = 8).

(F) Plasma cholesterol levels after 12 weeks of HFD feeding (n = 8).

(G) Plasma TG levels after 12 weeks of HFD feeding (n = 8).

(H) H&E staining of eWAT, iWAT, and BAT (n = 3). Scale bar, 100 μm in eWAT and iWAT, 50 μm in BAT.

(I) Quantification of adipocytes size in eWAT from three random fields across three slices.

(J) Quantification of adipocytes size in iWAT from three random fields across three slices.

(K and L) The Intraperitoneal Glucose Tolerance Test (ipGTT) curve (K) and area under the curve (L) after 10 weeks of HFD feeding (n = 6).

(M and N) The Insulin Tolerance Test (ITT) curve (M) and area under the curve (N) after 10 weeks of HFD feeding (n = 6).

(O) Experimental design outlining different temperatures used in metabolic cages: TN (28°C), RT (22°C), and CE (8°C).

(P–R) Analysis of covariance (ANCOVA) analysis of daily energy expenditure per body weight of mice housed at 28°C (P), 22°C (Q), and 8°C (R) (n = 5).

(legend continued on next page)

CellPress
OPEN ACCESS

(CE) conditions (Figure 5O). This experimental design allowed us to explore how *Medag* AKO influences metabolic flexibility and substrate utilization in response to environmental changes. Notably, AKO mice displayed increased energy expenditure at TN, a trend that decreased at RT and further diminished in CE (Figures 5P–5R). At TN, where thermogenic demand is minimal, the increased energy expenditure suggests that MEDAG modulates basal metabolic rate. In contrast, sequential activation of thermogenic mechanisms at RT and CE may shadow the AKO effect. Moreover, AKO mice exhibited a higher respiratory exchange ratio (RER) at RT and CE, but not at TN, indicating a shift toward increased carbohydrate utilization under these conditions (Figures 5S–5U). Therefore, increased reliance on carbohydrates could be responsible for lower blood glucose levels (Figures 5K and 5N), especially because the total food intake and locomotor activity are comparable in AKO and control mice (Figures S4D and S4E). These findings position adipose tissue *Medag* as a promising anti-obesity target without the risk of drastic metabolic perturbations.

PPARγ/GLUT signaling acts downstream of PKA activation in *Medag* AKO mice

We next sought to ascertain whether the physiological phenotypes of AKO mice arise from the mechanistic underpinnings seen in our *in vitro* system positioning MEDAG as an AKAP in brown adipocytes. To preclude the confounding effects of obesity in HFD-fed mice, we utilized chow-diet-fed AKO mice, which have body weights comparable to control mice 2 weeks after tamoxifen-induced KO (Figures 6A and 6B). The energy expenditure of chow-fed AKO mice at different temperatures showed a similar trend as the HFD-fed AKO mice with higher energy expenditure and RER at TN (Figures 6C–6F and S5A). Under RT, the increase in energy expenditure persisted, but without a preference for carbohydrates; both metrics normalized under CE (Figures S5B–S5I). Locomotor activity remained unchanged with increased food intake (Figures S5J and S5K). This compensatory feeding response likely offsets elevated energetic demands, explaining the absence of expected improvements in glucose tolerance and core temperature despite heightened EE. These findings confirmed that *Medag* deletion enhances energy expenditure predominantly through increased basal metabolic rate. Moreover, administration of the β3-adrenergic receptor agonist (CL316,243) did not further amplify the elevated EE in *Medag* AKO mice (Figures S5L–S5N). The magnitude of the EE increase remained comparable between basal and agonist-stimulated conditions in AKO mice. Notably, the statistical significance of EE elevation was reduced in CL316,243-treated mice due to injection-induced inter-individual variability. Intriguingly, AKO mice maintained lower blood glucose levels in fed states, but not during fasting (Figure 6G). In contrast, AKO mice showed elevated plasma fatty acids during overnight fasting but not in the fed state (Figure 6H). This indicates that AKO mice preferentially utilize glucose under fed conditions but switch to lipid utilization when glucose availability is low, demonstrating remarkable metabolic flexibility. Strikingly, this adaptive response recapitulates the cell-autonomous substrate flexibility observed in *Medag*-deficient brown adipocytes, where *Medag* KD enhanced basal glucose oxidation. Upon β-adrenergic stimulation, it comprehensively increased glucose oxidation along with increased FAs and glutamine utilization (Figures S2A and S2B).

To evaluate MEDAG's AKAP-like function *in vivo*, we analyzed PKA activity in adipose tissues of AKO mice following TN housing. AKO mice exhibited significantly elevated PKA activity in both iBAT and eWAT compared with WT controls (Figure 6I). This hyperactivation was accompanied by the downregulation of PKA-RIIβ protein levels in these depots (Figures 6J and 6K). Strikingly, downstream signaling diverged tissue-specifically. Specifically, iBAT showed a notable upregulation of P-CREB (Figure S5O). Conversely, eWAT showed an increase in P-HSL, suggesting enhanced lipolysis. iWAT showed no significant changes in PKA activity, pointing to the tissue-specific functions of *Medag* (Figures S5P and S5Q). Importantly, UCP-1 was elevated in iBAT but not in WAT, confirming a more metabolically active iBAT in AKO mice (Figure 6L). Transcriptional analyses further supported these findings. In iBAT, key thermogenic markers (*Prdm16* and *Ucp-1*) , lipid metabolism markers (*Elovl3* and *Pparγ*), and glucose metabolism markers (*Pparγ* and *Pepck*) were significantly elevated in AKO mice (Figure 6M).[36] Although transcriptional increases in these markers were noticed in eWAT, the lack of corresponding protein level elevations for UCP-1 suggests a limited involvement of eWAT in whole-body energy expenditure (Figure 6N).

To understand how AKO mice maintain lower blood glucose levels, we considered a plausible role for *Pparγ* upregulation (Figures 6M and 6N) and consequent regulation of glucose transporters. PPARγ plays a significant role in regulating glucose metabolism and insulin sensitivity through its regulatory effects in adipose tissue.[37] We observed a significant upregulation of PPARγ, glucose transporter 1 (GLUT1), and GLUT4 in iBAT, despite observed the downregulation of *Glut4* mRNA (Figures 6M and 6O). A lack of such a response in eWAT suggests a BAT-specific role (Figure 6P). Importantly, this regulation of glucose uptake appears to occur independently of insulin, as phosphorylated protein kinase B (P-AKT) levels in adipose tissues, as well as systemic insulin secretion and sensitivity, remain unchanged (Figures 5K–5N, 6O, and 6P). This suggests that *Medag*'s regulation bypasses classical insulin signaling. Consistently, in both human cohorts (cohort 1 and 2), we observed a consistent negative correlation between *MEDAG* expression and *GLUT1* expression in BAT (Figure 6Q). Additionally, in human WAT (cohort 3), *MEDAG* expression showed a negative correlation with both *PPARγ* and *GLUT4* (Figure 6R). These findings support the regulatory role of *MEDAG* in PPARγ/GLUT signaling.

(S–U) Daily RER in mice housed at 28°C (S), 22°C (T), and 8°C (U) ($n = 5$).
Data are presented as mean ± SEM. Statistical analysis was performed using unpaired two-tailed *t* test (B–G, I–N, T, and U) and ANCOVA analysis using body weight as a covariate (P–R). ns, not significant, $^{*}p < 0.05$, $^{**}p < 0.01$, $^{***}p < 0.001$, $^{****}p < 0.0001$.
See also Figure S4.

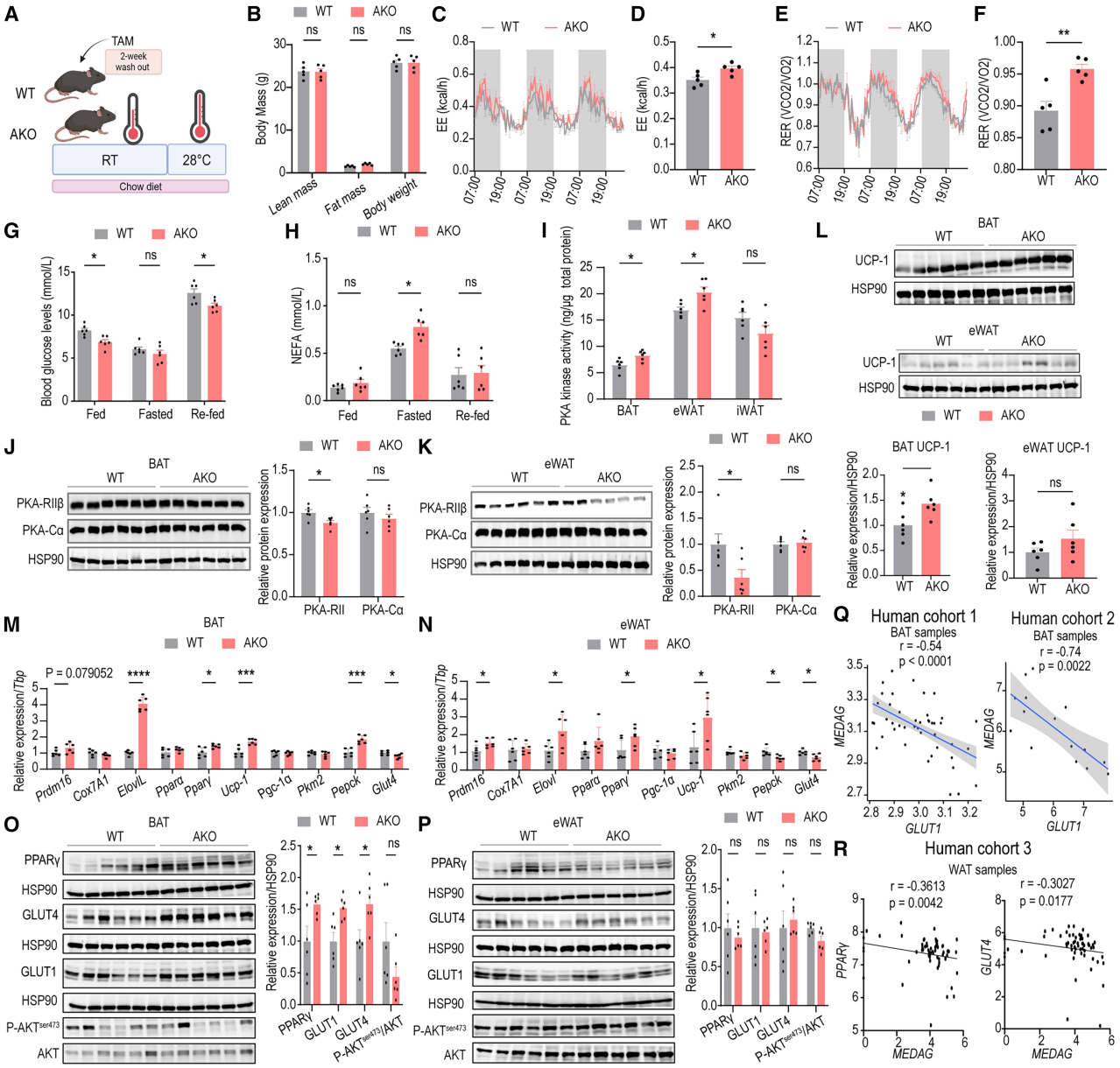

Figure 6. PPARγ/GLUT signaling acts downstream of PKA activation in *Medag* AKO mice

(A) Schematic illustration of experimental design: RT (22°C), TN conditions (28°C).

(B) Body composition and weight of mice 2 weeks after KO induction and wash out (n = 5).

(C and D) Energy expenditure curve and daily energy expenditure of mice housed at 28°C (n = 5).

(E and F) RER curve and daily RER of mice housed at 28°C (n = 5).

(G) Tail vein blood glucose levels were measured under fed conditions, after a 16-h fast and 2 h after re-feeding in mice housed at 28°C for 1 week (n = 6).

(H) Tail vein plasma NEFA levels were measured under fed conditions, after a 16-h fast and 2 h after re-feeding in mice housed at 28°C for 1 week (n = 6).

(I) PKA kinase activity of adipose depots from mice housed at 28°C for 1 week (n = 6).

(J) Representative blots and quantification of PKA-RIIβ and PKA-Cα protein levels in BAT from mice housed at 28°C for 1 week (n = 6).

(K) Representative blots and quantification of PKA-RIIβ and PKA-Cα protein levels in eWAT from mice housed at 28°C for 1 week (n = 6).

(L) Representative blots and quantification of UCP-1 protein levels in BAT and eWAT from mice housed at 28°C for 1 week (n = 6).

(M) Real-time qPCR of thermogenesis markers in BAT from mice housed at 28°C for 1 week (n = 6).

(N) Real-time qPCR of thermogenesis markers in eWAT from mice housed at 28°C for 1 week (n = 6).

(O and P) Representative blots and quantification of PPARγ, GLUT4, GLUT1, and P-AKT protein levels in BAT (O) and eWAT (P) from mice housed at 28°C for 1 week (n = 6).

(Q) Correlation analysis between normalized expression of *MEDAG* and *GLUT1* in bulk RNA-seq of BAT from human cohort 1 and 2 (n = 44 for left, 15 for right).

(legend continued on next page)

CellPress
OPEN ACCESS

DISCUSSION

Metabolic benefits of catabolic brown/beige adipocytes are arguably contingent upon their ability to increase EE.[38] Recent studies have highlighted additional benefit of these adipocytes beyond EE, underscoring their therapeutic potential.[13,14,39,40] To exploit this potential, we need to comprehensively identify and scrutinize potential targets, which poses multiple challenges such as tissue specificity, efficacy, and the nature of intervention needed to modulate the activity of the candidate. Consequently, most studies in recent years focused on the activation of catabolic adipocytes through the stimulation of UCP-1 or other positive regulators of catabolic adipocytes. In contrast, we identified *MEDAG* as the negative regulator of catabolic adipocyte activity, offering several conceivable advantages and ease of targetability through pharmacological and non-pharmacological means. Moreover, given that our findings are tested in human data and systematically validated in cellular and mouse models, the therapeutic relevance is particularly promising.

These findings also advance our basic understanding of BAT functioning, the regulation of PKA activity in adipocytes, and establish MEDAG as a unique AKAP. As components of cAMP-independent PKA signaling, AKAPs spatially confine the PKA signaling to specific cellular compartments. Among over 50 structurally diverse yet functionally similar AKAPs, all feature an amphipathic helix that binds the N-terminal dimerization/docking domain of PKA-R subunits.[24] We examined the structural binding of MEDAG to PKA-RIIβ subunits using computational prediction and observed a similar topological organization. However, experimentally solving the structure of this complex could yield further insights that could be exploited to pharmacologically modulate the MEDAG-PKA interaction. Moreover, it would be interesting to test the effect of pharmacological agents known to modulate PKA activity on MEDAG-PKA interaction. In addition, while we have validated the interaction using cellular methodology, measuring the precise binding affinity of phosphorylated, unphosphorylated, and mutant MEDAG to PKA-RIIβ using high-resolution biophysical methods will be important for deeper understanding of the interaction.

The timely extinction of PKA activity is as crucial as its apt activation. The spatiotemporally precise attenuation of the PKA signal is usually achieved by the hydrolysis of cAMP by phosphodiesterase or through the inhibition of free catalytic subunit by the heat-stable inhibitor PKI.[41] In contrast, the PKA activity modulation by MEDAG functions as a rheostat to preclude overactivation. MEDAG OE did not alter the basal activity of PKA but effectively inhibited overactivated PKA upon PKA-Cα OE. This may represent an inherent cellular mechanism to preclude PKA hyperactivity. We speculate that a stoichiometric binding or the PKA-mediated activation of MEDAG could be the key controlling mechanism. Regardless of the mechanistic intricacies, MEDAG upregulation in obesity and previously reported association of aberrant PKA signaling may imply a pathological role of ectopic MEDAG-PKA interaction.

Contrasting other AKAPs, MEDAG shows peculiar feedback regulatory loop interaction with PKA. Activated PKA phosphorylates MEDAG, which subsequently inhibits excessive PKA activation. Although molecular biology analyses confirmed phosphorylation, attempts to quantify the modification and mapping of phosphorylation site(s) with mass spectrometry were unsuccessful. In adipose tissue, D-AKAP1 is the primary AKAP anchoring PKA to lipid droplets, inhibiting fatty acid oxidation (FAO) and thermogenesis through acyl-CoA synthetase long-chain (ACSL) phosphorylation.[42] MEDAG seems to operate differently, likely to achieve a divergent function. Rather than anchoring PKA, MEDAG equilibrates the availability of RIIβ subunit, thus decoupling the PKA activity modulation from cAMP availability, unlike other AKAPs (such as D-AKAP2 and PRAJA2) showing specificity for RI and RII subunits.[43] Nevertheless, specificity of MEDAG toward RIIβ is consistent with the predominance of RIIβ in adipocytes.[21]

Consistent with the different R-subunit-binding partners, the downstream effects of PKA activity modulation by *Medag* in adipocytes diverge from known AKAPs (e.g., OPA1).[44] Loss-of-function studies in BAT emphasize the preferential effect of *Medag* on glucose uptake rather than lipolysis. This divergence reflects the capacity of AKAP-targeted PKA signaling to rewire metabolic priorities beyond classical lipolytic pathways. For instance, PKA activation can modulate vagal afferent firing to suppress hepatic glucose production[45] and engages general control non-derepressible 5 (GCN5)-CBP/p300-interacting transactivator with E/D-rich carboxy-terminal domain-2 (CITED2) complexes to redirect hepatic substrate utilization.[46] During thermogenesis, BAT, but not WAT, increases glucose uptake[47,48] for various, largely uncertain, metabolic fates, including lipogenesis,[49] energy source,[50,51] or auxiliary pathways.[52] In our metabolic studies in *Medag* AKO mice, we observed a systemic preference for carbohydrates as a fuel source, supporting its preferential use in energy production through PKA/PPARγ/GLUT signaling. Besides working downstream PKA/CREB signaling,[53] PPARγ directly regulates the expression of glucose uptake and insulin signaling-related genes with PPARγ agonists augmenting the expression of insulin receptor and GLUT4.[54] MEDAG likely modulates the subcellular localization of PKA to moderate metabolic glucose flux to meet acute ATP demand. In this context, modulation of insulin-independent glucose metabolism by adipose-specific *Medag* targeting open avenues for future explorations.

Overall, our study elucidates that MEDAG acts as an AKAP in catabolic adipocytes to modulate whole-body glucose homeostasis and energy expenditure. These findings position *Medag* as a promising therapeutic target to tackle obesity and metabolic disorders.

(R) Correlation analysis between normalized expression of *MEDAG* and *PPARγ* and *GLUT4* in bulk RNA-seq of WAT from human cohort 3 (n = 61).
Data are presented as mean ± SEM. Statistical analysis was performed using unpaired two-tailed t test (B, D, and F–P) and Spearman correlation coefficients (Q and R). ns, not significant, $^{*}p < 0.05$, $^{**}p < 0.01$, $^{***}p < 0.001$, $^{****}p < 0.0001$.
See also Figure S5.

Limitations

This study opens several interesting questions to be answered in future studies. First, a comprehensive assessment of the metabolic phenotype in global and tissue-specific *Medag* KO mice is essential. Second, structural insights into the MEDAG/PKA-RIIβ complex and its biophysical characterization is essential for effective targeting by disrupting the MEDAG-PKA-RIIβ interaction. Third, AKAP activity of endogenous MEDAG remains poorly defined, primarily due to antibody unavailability necessitating further biochemical and structural exploration of endogenous MEDAG and PKA. Last, given the range of PKA targets in different tissues and versatile expression of *Medag*, further research is required to elucidate the cell/tissue specificity of the MEDAG phenotype.

RESOURCE AVAILABILITY

Lead contact

Further information and requests for reagents and resources should be directed to and will be fulfilled by the lead contact, Christian Wolfrum (christian.wolfrum@ntu.edu.sg).

Materials availability

MEDAG AKO mice and plasmids generated in this study will be available from the lead contact without restriction.

Data and code availability

- Unprocessed and uncompressed imaging data have been deposited at Mendeley data: https://doi.org/10.17632/vctw9w8bhs.1. All data deposited will be publicly available as of the date of publication. The RNA-seq data from human cohort 1 are available at European Nucleotide Archive (ENA: PRJEB20634) and for cohort 2 at Gene Expression Omnibus (GEO: GSE220158). Cohorts 3 and 4 data cannot be deposited in a public repository due to patient consent and local data protection regulations. Access to cohort 3 datasets is available upon request from C. Wolfrum (christian.wolfrum@ntu.edu.sg) for non-commercial academic research purposes; no data use agreement is required. The bulk and snRNA-seq data from human cohort 4 can be accessed at https://github.com/WolfrumLab/MHUO (contact M. Blüher [matthias.blueher@medizin.uni-leipzig.de]) for approval by the steering committee. Access to the human cohort 4 dataset is regulated by the LOBB Steering Committee and requires approval of a data use agreement (DUA) specifying permitted research purposes and protections for participant privacy. Requests will be acknowledged within 5–10 business days and, following review, are typically approved or declined within 2–4 weeks, depending on application completeness and scope. Access is restricted to non-commercial, non-identifiable research use and may be granted to named researchers or institutions upon execution of a DUA via M. Blüher (matthias.blueher@medizin.uni-leipzig.de).
- This paper does not report original code.
- Any additional information required to reanalyze the data reported in this paper is available from the lead contact upon request.

ACKNOWLEDGMENTS

We thank Manuel Klug for his help with animal studies; Laboratory for Animal Model Pathology, University of Zurich for the histologic analysis; the ETH Phenomics Center and SLA Animal Facility for assistance in mouse husbandry; and the Scientific Center for Optical and Electron Microscopy of ETH for the microscopy facility. The work was supported by the Swiss National Science Foundation (SNSF) and Personalized Health and Related Technologies (PHRT). M. Balaz received funding from the European Union's Horizon 2020 research and innovation program under the Marie Skłodowska-Curie grant agreement no. 945478, the Slovak Research and Development Agency (grant no. APVV-22-0291), and VEGA (grant no. 2/0102/23). M. Blüher received funding from grants from the DFG Projektnummer 209933838—SFB 1052 (project B1) and from Deutsches Zentrum für Diabetesforschung (DZD, grant: 82DZD00601).

AUTHOR CONTRIBUTIONS

Conceptualization, C. Wolfrum and F.L.; methodology, F.L., A.K.S., A.G., and T.X.; investigation, F.L.; data acquisition and analysis, F.L., A.K.S., L.D., C. Wu, T.W., M. Balaz, and R.K.; human cohort data analysis, A.G.; human cohort 1 samples and data acquisition, P.S., L.V., and M. Balaz; human cohort 3 samples and data acquisition, V.G., B.D., L.A.-N., and J.R.R.; human cohort 4 samples and data acquisition, F.N., W.S., H.D., A.H., M. Blüher, and C. Wolfrum; computational simulation for MEDAG/PKA-RIIβ complex, T.X.; visualization, F.L., A.G., and A.K.S.; funding acquisition, C. Wolfrum; supervision, A.K.S. and C. Wolfrum; writing – original draft, F.L. and A.K.S.; writing – review & editing, F.L., M. Balaz, A.G., J.R.R., A.K.S., and C. Wolfrum.

DECLARATION OF INTERESTS

M. Blüher received honoraria as a consultant and speaker from Amgen, AstraZeneca, Bayer, Boehringer Ingelheim, Daiichi-Sankyo, Lilly, Novo Nordisk, Novartis, Pfizer and Sanofi.

STAR★METHODS

Detailed methods are provided in the online version of this paper and include the following:

- KEY RESOURCES TABLE
- EXPERIMENTAL MODEL AND STUDY PARTICIPANT DETAILS
  - Clinical sample acquisition of human adipose tissue
  - Mice experiments
  - Cell culture-immortalized murine brown adipocytes
  - Cell culture-3T3-L1
- METHOD DETAILS
  - Clinical transcriptome study cohorts
  - Intraperitoneal Glucose Tolerance Test
  - Intraperitoneal Insulin Tolerance Test
  - Body composition measurement
  - Indirect Calorimetry
  - Tissue Harvest
  - Cellular Respiration and Glycolytic Stress Test
  - Lipolysis
  - RNA extraction, cDNA synthesis, Quantitative RT-PCR
  - Protein extraction and western blot
  - Molecular cloning
  - Lentivirus packaging
  - CO- Immunoprecipitation (CO-IP)
  - Dot blot overlay assay
  - Immunofluorescence
  - Computational prediction of MEDAG-PKA-RIIβ dimer complex structure
  - Histological staining
  - Plasma TG, FFA and cholesterol measurements
  - cAMP levels and PKA kinase activity measurements
- QUANTIFICATION AND STATISTICAL ANALYSIS

SUPPLEMENTAL INFORMATION

Supplemental information can be found online at https://doi.org/10.1016/j.molcel.2026.02.001.

Received: January 29, 2025
Revised: October 21, 2025
Accepted: February 2, 2026
Published: February 25, 2026

REFERENCES

1. Blüher, M. (2019). Obesity: global epidemiology and pathogenesis. Nat. Rev. Endocrinol. *15*, 288–298. https://doi.org/10.1038/s41574-019-0176-8.
2. Hall, K.D., and Guo, J. (2017). Obesity Energetics: Body Weight Regulation and the Effects of Diet Composition. Gastroenterology *152*, 1718–1727.e3. https://doi.org/10.1053/j.gastro.2017.01.052.
3. Leiria, L.O., Wang, C.-H., Lynes, M.D., Yang, K., Shamsi, F., Sato, M., Sugimoto, S., Chen, E.Y., Bussberg, V., Narain, N.R., et al. (2019). 12-Lipoxygenase Regulates Cold Adaptation and Glucose Metabolism by Producing the Omega-3 Lipid 12-HEPE from Brown Fat. Cell Metab. *30*, 768–783.e7. https://doi.org/10.1016/j.cmet.2019.07.001.
4. Lynes, M.D., Leiria, L.O., Lundh, M., Bartelt, A., Shamsi, F., Huang, T.L., Takahashi, H., Hirshman, M.F., Schlein, C., Lee, A., et al. (2017). The cold-induced lipokine 12,13-diHOME promotes fatty acid transport into brown adipose tissue. Nat. Med. *23*, 631–637. https://doi.org/10.1038/nm.4297.
5. Stanford, K.I., Middelbeek, R.J.W., Townsend, K.L., An, D., Nygaard, E.B., Hitchcox, K.M., Markan, K.R., Nakano, K., Hirshman, M.F., Tseng, Y.-H., et al. (2013). Brown adipose tissue regulates glucose homeostasis and insulin sensitivity. J. Clin. Investig. *123*, 215–223. https://doi.org/10.1172/JCI62308.
6. Shi, M., Huang, X.-Y., Ren, X.-Y., Wei, X.-Y., Ma, Y., Lin, Z.-Z., Liu, D.-T., Song, L., Zhao, T.-J., Li, G., et al. (2021). AIDA directly connects sympathetic innervation to adaptive thermogenesis by UCP1. Nat. Cell Biol. *23*, 268–277. https://doi.org/10.1038/s41556-021-00642-9.
7. Sakers, A., De Siqueira, M.K., Seale, P., and Villanueva, C.J. (2022). Adipose-tissue plasticity in health and disease. Cell *185*, 419–446. https://doi.org/10.1016/j.cell.2021.12.016.
8. Wu, J., Boström, P., Sparks, L.M., Ye, L., Choi, J.H., Giang, A.-H., Khandekar, M., Virtanen, K.A., Nuutila, P., Schaart, G., et al. (2012). Beige Adipocytes Are a Distinct Type of Thermogenic Fat Cell in Mouse and Human. Cell *150*, 366–376. https://doi.org/10.1016/j.cell.2012.05.016.
9. Virtanen, K.A., Lidell, M.E., Orava, J., Heglind, M., Westergren, R., Niemi, T., Taittonen, M., Laine, J., Savisto, N.-J., Enerbäck, S., et al. (2009). Functional Brown Adipose Tissue in Healthy Adults. N. Engl. J. Med. *360*, 1518–1525. https://doi.org/10.1056/NEJMoa0808949.
10. Cypess, A.M., Lehman, S., Williams, G., Tal, I., Rodman, D., Goldfine, A.B., Kuo, F.C., Palmer, E.L., Tseng, Y.-H., Doria, A., et al. (2009). Identification and importance of brown adipose tissue in adult humans. N. Engl. J. Med. *360*, 1509–1517. https://doi.org/10.1056/NEJMoa0810780.
11. van Marken Lichtenbelt, W.D. van M., Vanhommerig, J.W., Smulders, N.M., Drossaerts, J.M.A.F.L., Kemerink, G.J., Bouvy, N.D., Schrauwen, P., and Teule, G.J.J. (2009). Cold-Activated Brown Adipose Tissue in Healthy Men. N. Engl. J. Med. *360*, 1500–1508. https://doi.org/10.1056/NEJMoa0808718.
12. Jurado-Fasoli, L., Sanchez-Delgado, G., Alcantara, J.M.A., Acosta, F.M., Sanchez-Sanchez, R., Labayen, I., Ortega, F.B., Martinez-Tellez, B., and Ruiz, J.R. (2024). Adults with metabolically healthy overweight or obesity present more brown adipose tissue and higher thermogenesis than their metabolically unhealthy counterparts. EBioMedicine *100*, 104948. https://doi.org/10.1016/j.ebiom.2023.104948.
13. Vargas-Castillo, A., Sun, Y., Smythers, A.L., Grauvogel, L., Dumesic, P.A., Emont, M.P., Tsai, L.T., Rosen, E.D., Zammit, N.W., Shaffer, S.M., et al. (2024). Development of a functional beige fat cell line uncovers independent subclasses of cells expressing UCP1 and the futile creatine cycle. Cell Metab. *36*, 2146–2155.e5. https://doi.org/10.1016/j.cmet.2024.07.002.
14. Wang, T., Sharma, A.K., Wu, C., Maushart, C.I., Ghosh, A., Yang, W., Stefanicka, P., Kovanicova, Z., Ukropec, J., Zhang, J., et al. (2024). Single-nucleus transcriptomics identifies separate classes of UCP1 and futile cycle adipocytes. Cell Metab. *36*, 2130–2145.e7. https://doi.org/10.1016/j.cmet.2024.07.005.
15. Becher, T., Palanisamy, S., Kramer, D.J., Eljalby, M., Marx, S.J., Wibmer, A.G., Butler, S.D., Jiang, C.S., Vaughan, R., Schöder, H., et al. (2021). Brown adipose tissue is associated with cardiometabolic health. Nat. Med. *27*, 58–65. https://doi.org/10.1038/s41591-020-1126-7.
16. London, E., and Stratakis, C.A. (2022). The regulation of PKA signaling in obesity and in the maintenance of metabolic health. Pharmacol. Ther. *237*, 108113. https://doi.org/10.1016/j.pharmthera.2022.108113.
17. London, E., Bloyd, M., and Stratakis, C.A. (2020). PKA functions in metabolism and resistance to obesity: lessons from mouse and human studies. J. Endocrinol. *246*, R51–R64. https://doi.org/10.1530/JOE-20-0035.
18. Favaro, E., Granata, R., Miceli, I., Baragli, A., Settanni, F., Cavallo Perin, P., Ghigo, E., Camussi, G., and Zanone, M.M. (2012). The ghrelin gene products and exendin-4 promote survival of human pancreatic islet endothelial cells in hyperglycaemic conditions, through phosphoinositide 3-kinase/Akt, extracellular signal-related kinase (ERK)1/2 and cAMP/protein kinase A (PKA) signalling pathways. Diabetologia *55*, 1058–1070. https://doi.org/10.1007/s00125-011-2423-y.
19. Zhang, P., Smith-Nguyen, E.V., Keshwani, M.M., Deal, M.S., Kornev, A.P., and Taylor, S.S. (2012). Structure and allostery of the PKA RIIβ tetrameric holoenzyme. Science *335*, 712–716. https://doi.org/10.1126/science.1213979.
20. Mantovani, G., Bondioni, S., Alberti, L., Gilardini, L., Invitti, C., Corbetta, S., Zappa, M.A., Ferrero, S., Lania, A.G., Bosari, S., et al. (2009). Protein kinase A regulatory subunits in human adipose tissue: decreased R2B expression and activity in adipocytes from obese subjects. Diabetes *58*, 620–626. https://doi.org/10.2337/db08-0585.
21. Cummings, D.E., Brandon, E.P., Planas, J.V., Motamed, K., Idzerda, R.L., and McKnight, G.S. (1996). Genetically lean mice result from targeted disruption of the RII beta subunit of protein kinase A. Nature *382*, 622–626. https://doi.org/10.1038/382622a0.
22. Karin, M., and Hunter, T. (1995). Transcriptional control by protein phosphorylation: signal transmission from the cell surface to the nucleus. Curr. Biol. *5*, 747–757. https://doi.org/10.1016/S0960-9822(95)00151-5.
23. Bock, A., Annibale, P., Konrad, C., Hannawacker, A., Anton, S.E., Maiellaro, I., Zabel, U., Sivaramakrishnan, S., Falcke, M., and Lohse, M.J. (2020). Optical Mapping of cAMP Signaling at the Nanometer Scale. Cell *182*, 1519–1530.e17. https://doi.org/10.1016/j.cell.2020.07.035.
24. Colledge, M., and Scott, J.D. (1999). AKAPs: from structure to function. Trends Cell Biol. *9*, 216–221. https://doi.org/10.1016/s0962-8924(99)01558-5.
25. Wong, W., and Scott, J.D. (2004). AKAP signalling complexes: focal points in space and time. Nat. Rev. Mol. Cell Biol. *5*, 959–970. https://doi.org/10.1038/nrm1527.
26. Zhang, H., Chen, X., and Sairam, M.R. (2012). Novel genes of visceral adiposity: identification of mouse and human mesenteric estrogen-dependent adipose (MEDA)-4 gene and its adipogenic function. Endocrinology *153*, 2665–2676. https://doi.org/10.1210/en.2011-2008.
27. Maushart, C.I., Sun, W., Othman, A., Ghosh, A., Senn, J.R., Fischer, J.G.W., Madoerin, P., Loeliger, R.C., Benz, R.M., Takes, M., et al. (2023). Effect of high-dose glucocorticoid treatment on human brown adipose tissue activity: a randomised, double-blinded, placebo-controlled cross-over trial in healthy men. EBioMedicine *96*, 104771. https://doi.org/10.1016/j.ebiom.2023.104771.
28. Martinez-Tellez, B., Sanchez-Delgado, G., Acosta, F.M., Alcantara, J.M.A., Amaro-Gahete, F.J., Martinez-Avila, W.D., Merchan-Ramirez, E., Muñoz-Hernandez, V., Osuna-Prieto, F.J., Jurado-Fasoli, L., et al. (2022). No evidence of brown adipose tissue activation after 24 weeks of supervised exercise training in young sedentary adults in the ACTIBATE randomized controlled trial. Nat. Commun. *13*, 5259. https://doi.org/10.1038/s41467-022-32502-x.
29. Emont, M.P., Jacobs, C., Essene, A.L., Pant, D., Tenen, D., Colleluori, G., Di Vincenzo, A., Jørgensen, A.M., Dashti, H., Stefek, A., et al. (2022). A

single-cell atlas of human and mouse white adipose tissue. Nature *603*, 926–933. https://doi.org/10.1038/s41586-022-04518-2.

30. Reinisch, I., Ghosh, A., Noé, F., Sun, W., Dong, H., Leary, P., Dietrich, A., Hoffmann, A., Blüher, M., and Wolfrum, C. (2025). Unveiling adipose populations linked to metabolic health in obesity. Cell Metab. *37*, 640–655.e4. https://doi.org/10.1016/j.cmet.2024.11.006.
31. Walley, A.J., Jacobson, P., Falchi, M., Bottolo, L., Andersson, J.C., Petretto, E., Bonnefond, A., Vaillant, E., Lecoeur, C., Vatin, V., et al. (2012). Differential coexpression analysis of obesity-associated networks in human subcutaneous adipose tissue. Int. J. Obes. (Lond) *36*, 137–147. https://doi.org/10.1038/ijo.2011.22.
32. Shaywitz, A.J., and Greenberg, M.E. (1999). CREB: a stimulus-induced transcription factor activated by a diverse array of extracellular signals. Annu. Rev. Biochem. *68*, 821–861. https://doi.org/10.1146/annurev.biochem.68.1.821.
33. Arias, J., Alberts, A.S., Brindle, P., Claret, F.X., Smeal, T., Karin, M., Feramisco, J., and Montminy, M. (1994). Activation of cAMP and mitogen responsive genes relies on a common nuclear factor. Nature *370*, 226–229. https://doi.org/10.1038/370226a0.
34. Martínez-Férriz, A., Ferrando, A., Fathinajafabadi, A., and Farràs, R. (2022). Ubiquitin-mediated mechanisms of translational control. Semin. Cell Dev. Biol. *132*, 146–154. https://doi.org/10.1016/j.semcdb.2021.12.009.
35. Lignitto, L., Carlucci, A., Sepe, M., Stefan, E., Cuomo, O., Nisticò, R., Scorziello, A., Savoia, C., Garbi, C., Annunziato, L., et al. (2011). Control of PKA stability and signalling by the RING ligase praja2. Nat. Cell Biol. *13*, 412–422. https://doi.org/10.1038/ncb2209.
36. Zhang, Z., Yang, D., Xiang, J., Zhou, J., Cao, H., Che, Q., Bai, Y., Guo, J., and Su, Z. (2021). Non-shivering Thermogenesis Signalling Regulation and Potential Therapeutic Applications of Brown Adipose Tissue. Int. J. Biol. Sci. *17*, 2853–2870. https://doi.org/10.7150/ijbs.60354.
37. Picard, F., and Auwerx, J. (2002). PPAR(gamma) and glucose homeostasis. Annu. Rev. Nutr. *22*, 167–197. https://doi.org/10.1146/annurev.nutr.22.010402.102808.
38. Fernández-Verdejo, R., Marlatt, K.L., Ravussin, E., and Galgani, J.E. (2019). Contribution of brown adipose tissue to human energy metabolism. Mol. Aspects Med. *68*, 82–89. https://doi.org/10.1016/j.mam.2019.07.003.
39. Verkerke, A.R.P., Wang, D., Yoshida, N., Taxin, Z.H., Shi, X., Zheng, S., Li, Y., Auger, C., Oikawa, S., Yook, J.-S., et al. (2024). BCAA-nitrogen flux in brown fat controls metabolic health independent of thermogenesis. Cell *187*, 2359–2374.e18. https://doi.org/10.1016/j.cell.2024.03.030.
40. Kajimura, S., Spiegelman, B.M., and Seale, P. (2015). Brown and Beige Fat: Physiological Roles beyond Heat Generation. Cell Metab. *22*, 546–559. https://doi.org/10.1016/j.cmet.2015.09.007.
41. Wen, W., Meinkoth, J.L., Tsien, R.Y., and Taylor, S.S. (1995). Identification of a signal for rapid export of proteins from the nucleus. Cell *82*, 463–473. https://doi.org/10.1016/0092-8674(95)90435-2.
42. Ji, L., Zhao, Y., He, L., Zhao, J., Gao, T., Liu, F., Qi, B., Kang, F., Wang, G., Zhao, Y., et al. (2021). AKAP1 Deficiency Attenuates Diet-Induced Obesity and Insulin Resistance by Promoting Fatty Acid Oxidation and Thermogenesis in Brown Adipocytes. Adv. Sci. (Weinh) *8*, 2002794. https://doi.org/10.1002/advs.202002794.
43. Kennedy, E.J., and Scott, J.D. (2015). Selective Disruption of the AKAP Signaling Complexes. Methods Mol. Biol. *1294*, 137–150. https://doi.org/10.1007/978-1-4939-2537-7_11.
44. Rogne, M., Chu, D.-T., Küntziger, T.M., Mylonakou, M.-N., Collas, P., and Tasken, K. (2018). OPA1-anchored PKA phosphorylates perilipin 1 on S522 and S497 in adipocytes differentiated from human adipose stem cells. Mol. Biol. Cell *29*, 1487–1501. https://doi.org/10.1091/mbc.E17-09-0538.
45. Rasmussen, B.A., Breen, D.M., Luo, P., Cheung, G.W.C., Yang, C.S., Sun, B., Kokorovic, A., Rong, W., and Lam, T.K.T. (2012). Duodenal activation of cAMP-dependent protein kinase induces vagal afferent firing and lowers glucose production in rats. Gastroenterology *142*, 834–843.e3. https://doi.org/10.1053/j.gastro.2011.12.053.
46. Sakai, M., Tujimura-Hayakawa, T., Yagi, T., Yano, H., Mitsushima, M., Unoki-Kubota, H., Kaburagi, Y., Inoue, H., Kido, Y., Kasuga, M., et al. (2016). The GCN5-CITED2-PKA signalling module controls hepatic glucose metabolism through a cAMP-induced substrate switch. Nat. Commun. *7*, 13147. https://doi.org/10.1038/ncomms13147.
47. Weir, G., Ramage, L.E., Akyol, M., Rhodes, J.K., Kyle, C.J., Fletcher, A.M., Craven, T.H., Wakelin, S.J., Drake, A.J., Gregoriades, M.-L., et al. (2018). Substantial Metabolic Activity of Human Brown Adipose Tissue during Warm Conditions and Cold-Induced Lipolysis of Local Triglycerides. Cell Metab. *27*, 1348–1355.e4. https://doi.org/10.1016/j.cmet.2018.04.020.
48. Bornstein, M.R., Neinast, M.D., Zeng, X., Chu, Q., Axsom, J., Thorsheim, C., Li, K., Blair, M.C., Rabinowitz, J.D., and Arany, Z. (2023). Comprehensive quantification of metabolic flux during acute cold stress in mice. Cell Metab. *35*, 2077–2092.e6. https://doi.org/10.1016/j.cmet.2023.09.002.
49. Sanchez-Gurmaches, J., Tang, Y., Jespersen, N.Z., Wallace, M., Martinez Calejman, C., Gujja, S., Li, H., Edwards, Y.J.K., Wolfrum, C., Metallo, C.M., et al. (2018). Brown Fat AKT2 Is a Cold-Induced Kinase that Stimulates ChREBP-Mediated De Novo Lipogenesis to Optimize Fuel Storage and Thermogenesis. Cell Metab. *27*, 195–209.e6. https://doi.org/10.1016/j.cmet.2017.10.008.
50. Lee, P., Bova, R., Schofield, L., Bryant, W., Dieckmann, W., Slattery, A., Govendir, M.A., Emmett, L., and Greenfield, J.R. (2016). Brown Adipose Tissue Exhibits a Glucose-Responsive Thermogenic Biorhythm in Humans. Cell Metab. *23*, 602–609. https://doi.org/10.1016/j.cmet.2016.02.007.
51. Li, M., Li, L., Li, B., Hambly, C., Wang, G., Wu, Y., Jin, Z., Wang, A., Niu, C., Wolfrum, C., et al. (2021). Brown adipose tissue is the key depot for glucose clearance in microbiota depleted mice. Nat. Commun. *12*, 4725. https://doi.org/10.1038/s41467-021-24659-8.
52. Jung, S.M., Doxsey, W.G., Le, J., Haley, J.A., Mazuecos, L., Luciano, A.K., Li, H., Jang, C., and Guertin, D.A. (2021). In vivo isotope tracing reveals the versatility of glucose as a brown adipose tissue substrate. Cell Rep. *36*, 109459. https://doi.org/10.1016/j.celrep.2021.109459.
53. Herzig, S., Hedrick, S., Morantte, I., Koo, S.-H., Galimi, F., and Montminy, M. (2003). CREB controls hepatic lipid metabolism through nuclear hormone receptor PPAR-gamma. Nature *426*, 190–193. https://doi.org/10.1038/nature02110.
54. Armoni, M., Harel, C., and Karnieli, E. (2007). Transcriptional regulation of the *GLUT4* gene: from PPAR-γ and FOXO1 to FFA and inflammation. Trends Endocrinol. Metab. *18*, 100–107. https://doi.org/10.1016/j.tem.2007.02.001.
55. Klein, J., Fasshauer, M., Klein, H.H., Benito, M., and Kahn, C.R. (2002). Novel adipocyte lines from brown fat: a model system for the study of differentiation, energy metabolism, and insulin action. BioEssays *24*, 382–388. https://doi.org/10.1002/bies.10058.
56. Wunderling, K., Zurkovic, J., Zink, F., Kuerschner, L., and Thiele, C. (2023). Triglyceride cycling enables modification of stored fatty acids. Nat. Metab. *5*, 699–709. https://doi.org/10.1038/s42255-023-00769-z.
57. Rosenwald, M., Perdikari, A., Rülicke, T., and Wolfrum, C. (2013). Bi-directional interconversion of brite and white adipocytes. Nat. Cell Biol. *15*, 659–667. https://doi.org/10.1038/ncb2740.
58. Turelli, P., Playfoot, C., Grun, D., Raclot, C., Pontis, J., Coudray, A., Thorball, C., Duc, J., Pankevich, E.V., Deplancke, B., et al. (2020). Primate-restricted KRAB zinc finger proteins and target retrotransposons control gene expression in human neurons. Sci. Adv. *6*, eaba3200. https://doi.org/10.1126/sciadv.aba3200.
59. Witwicka, H., Hwang, S.-Y., Reyes-Gutierrez, P., Jia, H., Odgren, P.E., Donahue, L.R., Birnbaum, M.J., and Odgren, P.R. (2015). Studies of OC-STAMP in Osteoclast Fusion: A New Knockout Mouse Model, Rescue of Cell Fusion, and Transmembrane Topology. PLoS One *10*, e0128275. https://doi.org/10.1371/journal.pone.0128275.

60. Sanchez-Delgado, G., Martinez-Tellez, B., Olza, J., Aguilera, C.M., Labayen, I., Ortega, F.B., Chillon, P., Fernandez-Reguera, C., Alcantara, J.M.A., Martinez-Avila, W.D., et al. (2015). Activating brown adipose tissue through exercise (ACTIBATE) in young adults: Rationale, design and methodology. Contemp. Clin. Trials *45*, 416–425. https://doi.org/10.1016/j.cct.2015.11.004.

61. Picelli, S., Faridani, O.R., Björklund, A.K., Winberg, G., Sagasser, S., and Sandberg, R. (2014). Full-length RNA-seq from single cells using Smart-seq2. Nat. Protoc. *9*, 171–181. https://doi.org/10.1038/nprot.2014.006.

62. Alpern, D., Gardeux, V., Russeil, J., Mangeat, B., Meireles-Filho, A.C.A., Breysse, R., Hacker, D., and Deplancke, B. (2019). BRB-seq: ultra-affordable high-throughput transcriptomics enabled by bulk RNA barcoding and sequencing. Genome Biol. *20*, 71. https://doi.org/10.1186/s13059-019-1671-x.

63. Wu, Y., Li, Q., and Chen, X.-Z. (2007). Detecting protein–protein interactions by far western blotting. Nat. Protoc. *2*, 3278–3284. https://doi.org/10.1038/nprot.2007.459.

64. Abramson, J., Adler, J., Dunger, J., Evans, R., Green, T., Pritzel, A., Ronneberger, O., Willmore, L., Ballard, A.J., Bambrick, J., et al. (2024). Accurate structure prediction of biomolecular interactions with AlphaFold 3. Nature *630*, 493–500. https://doi.org/10.1038/s41586-024-07487-w.

STAR★METHODS

KEY RESOURCES TABLE

REAGENT or RESOURCE	SOURCE	IDENTIFIER
Antibodies		
Rabbit polyclonal anti-HSL	Cell Signaling Technology	Cat# 4107; RRID: AB_2296900
Rabbit polyclonal anti-Phospho-HSL (Ser660)	Cell Signaling Technology	Cat# 4126; RRID: AB_490997
Rabbit monoclonal anti-HSP90	Cell Signaling Technology	Cat# 4877; RRID: AB_2233307
Rabbit monoclonal anti-Phospho-CREB (Ser133)	Cell Signaling Technology	Cat# 9198; RRID: AB_2561044
Rabbit monoclonal anti-CREB	Cell Signaling Technology	Cat# 9197; RRID: AB_331277
Rabbit polyclonal anti-PKA Cα	Cell Signaling Technology	Cat# 4782; RRID: AB_2170170
Rabbit monoclonal anti-HA Tag	Cell Signaling Technology	Cat# 3724; RRID: AB_1549585
Rabbit monoclonal anti-Flag Tag	Cell Signaling Technology	Cat# 14793; RRID: AB_2572291
Rabbit monoclonal anti-V5 Tag	Cell Signaling Technology	Cat# 13202; RRID: AB_2687461
Rabbit polyclonal anti-PKA-RIIβ	Proteintech	Cat# 28351-1-AP; RRID: AB_2918156
Rabbit polyclonal anti-PKA-RIα	Biorbyt	Cat# orb214438
Mouse polyclonal anti-PRAJA2	Invitrogen	Cat# PA5-69216; RRID: AB_2689996
Mouse monoclonal anti-Flag Tag	Cell Signaling Technology	Cat# 8146; RRID: AB_10950495
Rabbit monoclonal anti-Phospho-PKA Substrate	Cell Signaling Technology	Cat# 9624; RRID: AB_331817
Rabbit polyclonal anti-UCP1	Abcam	Ab10983; RRID: AB_2241462
Rabbit monoclonal anti-PPARγ	Cell Signaling Technology	Cat# 2443; RRID: AB_823598
Rabbit polyclonal anti-GLUT1	Abcam	Cat# Ab652; RRID: AB_305540
Mouse monoclonal anti-GLUT4	Cell Signaling Technology	Cat# 2213; RRID: AB_823508
Rabbit monoclonal anti-Phospho-Akt (Ser473)	Cell Signaling Technology	Cat# 4060; RRID: AB_2315049
Rabbit monoclonal anti-Phospho-Akt (Thr308)	Cell Signaling Technology	Cat# 13038; RRID: AB_2629447
Rabbit polyclonal anti-Akt	Cell Signaling Technology	Cat# 9272; RRID: AB_329827
Rabbit polyclonal anti-ATGL	Cell Signaling Technology	Cat# 2138; RRID: AB_2167955
Rabbit monoclonal anti-PGC-1α	Cell Signaling Technology	Cat# 2178; RRID: AB_823600
Rabbit monoclonal anti-Phospho-AMPKα (Thr172)	Cell Signaling Technology	Cat# 2535; RRID: AB_331250
Rabbit monoclonal anti-AMPKα	Cell Signaling Technology	Cat# 5831; RRID: AB_10622186
Rabbit monoclonal anti-PI3-K	Cell Signaling Technology	Cat# 4249; RRID: AB_2165248
Rabbit polyclonal anti-Phospho-IRS-1 (Ser612)	Cell Signaling Technology	Cat# 2386; RRID: AB_330326
Rabbit polyclonal anti-IRS-1	Cell Signaling Technology	Cat# 2382; RRID: AB_330333
Rabbit monoclonal anti-K48-linkage specific polyubiquitin	Cell Signaling Technology	Cat# 8081; RRID: AB_10859893
anti-mouse HRP secondary	Millipore	Cat# 401253; RRID: AB_437779
anti-rabbit HRP secondary	Millipore	Cat# 401393; RRID: AB_10683386
Goat anti-Mouse IgG (H+L) Superclonal™ Secondary Antibody, Alexa Fluor™ 488	Invitrogen	Cat# A28175; RRID: AB_2536161
Goat anti-Rabbit IgG (H+L) Cross-Adsorbed Secondary Antibody, Alexa Fluor™ 488	Invitrogen	Cat# A-11008; RRID: AB_143165
Goat anti-Rabbit IgG (H+L) Cross-Adsorbed Secondary Antibody, Alexa Fluor™ 568	Invitrogen	Cat# A-11011; RRID: AB_143157
Bacterial and virus strains		
plenti-PKA-RIIβ-V5	This paper	N/A
pLenti-PKA-Cα-HA	This paper	N/A
plenti-MEDAG^{wildtype}-FLAG	This paper	N/A
plenti-MEDAG^{251A}-FLAG	This paper	N/A

(*Continued on next page*)

CellPress
OPEN ACCESS

Continued

REAGENT or RESOURCE	SOURCE	IDENTIFIER
plenti-MEDAG^{251D}-FLAG	This paper	N/A
Biological samples		
Human BAT and subcutaneous WAT (human cohort 1)	University Hospital in Bratislava, Slovakia	N/A
Human BAT (human cohort 2)	University Hospital, Basel, Switzerland.	ClinicalTrials.gov ID: NCT03269747
Human subcutaneous WAT (human cohort 3)	University of Granada, Spain	ClinicalTrials.gov ID: NCT02365129
Human subcutaneous WAT (human cohort 4)	Leipzig Obesity Biobank, Germany	https://www.helmholtz-munich.de/en/diabetes-center/hi-mag/clinical-studies/leipzig-obesity-bio-bank-lobb
Chemicals, peptides, and recombinant proteins		
Hoechst33342	Cell Signaling Technology	Cat# 4082
HCS LipidTOX™ Deep Red Neutral Lipid Stain, for cellular imaging	Invitrogen	Cat# H34477
RNAiMAX Transfection Reagent	Thermo Fischer	Cat# 13778150
3-Isobutyl-1-methylxanthine	Sigma-Aldrich	Cat# I5879
Dexamethasone	Sigma-Aldrich	Cat# D4902
Indomethacin	Sigma-Aldrich	Cat# I7378
Insulin	Sigma-Aldrich	Cat# I9278
Rosiglitazone	Adipogen	Cat# 71740
Triiodo-L-Thyronine(T3)	Sigma-Aldrich	Cat# T6397
CL-316,243	Sigma-Aldrich	Cat# C5976
Collagen,Type I	Sigma-Aldrich	Cat# C3867
DMEM, low glucose	Lonza	Cat# BE12-707F
Penicillin-Streptomycin	Gibco	Cat# 15070063
DMEM, high glucose	Gibco	Cat# 41965062
Opti-MEM I reduced serum	Gibco	Cat# 31985062
L-glutamine	Gibco	Cat# 25030-024
Trizol reagent	Invitrogen	Cat# 15596026
DNaseI (RNase-free)	NEB	Cat# M0303
Forskolin	Sigma-Aldrich	Cat# 6886
Tamoxifen	Sigma-Aldrich	Cat# T5648
D-glucose	Sigma-Aldrich	Cat# G7021
Oligomycin	Adipogen	Cat# 11342
Isoproterenol	Sigma-Aldrich	Cat# I5627
Dibutyryl-cAMP	Sigma-Aldrich	Cat# D0627
FCCP	Sigma-Aldrich	Cat# C2920
Rotenone	Sigma-Aldrich	Cat# R8875
AntimycinA	Sigma-Aldrich	Cat# A8674
H89	MCE	Cat# HY-15979
Seahorse XF Base Medium	Agilent	Cat# 102353
Complete Protease Inhibitors	Roche	Cat# 05056489001
Halt Phosphatase Inhibitors	Thermo Fischer	Cat# 78426
PEG-it Virus precipitation solution	Bio Cat	Cat# LV825A-1-SBI
V5 Peptide	Sigma-Aldrich	Cat# V7754
3xFLAG™ Peptide	Sigma-Aldrich	Cat# F4799
Anti-FLAG M2 Affinity Gel	Sigma-Aldrich	Cat# A2220
Anti-V5 Agarose Affinity Gel	Sigma-Aldrich	Cat# A7345
Monoclonal Anti-HA-Agarose	Sigma-Aldrich	Cat# A2095

(*Continued on next page*)

Continued

REAGENT or RESOURCE	SOURCE	IDENTIFIER
InstantBlue Coomassie Protein Stain	Abcam	Cat# ab119211
Critical commercial assays		
DC Protein Assay	Bio-Rad	Cat# 5000111
High-Capacity cDNA RT kit	Applied Biosystems	N/A
Glycerol reagent	Sigma-Aldrich	Cat# F6428
XFE96 FluxPak	Agilent	Cat# 102416-100
PKA kinase activity kit	Enzo Life Sciences	Cat# ADI-EKS-390A
cAMP ELISA kit	Enzo Life Sciences	Cat# ADI-900-067A
SuperSep™ Phos-tag™ Precast Gels	Fujifilm	Cat# 195-17991
Zeba™ Spin Desalting Columns, 7K MWCO	Thermo Fischer	Cat# 89883
Deposited data		
Unprocessed and uncompressed imaging data	Mendeley Data	https://doi.org/10.17632/vctw9w8bhs.1
Human BAT and subcutaneous WAT (human cohort 1)	European Nucleotide Archive	accession code: PRJEB20634
Human BAT (human cohort 2)	Gene Expression Omnibus	accession code: GSE220158
Experimental models: Cell lines		
HEK293-LTV	Cell Biolabs	Cat# LTV-100
HEK293	ATCC	Cat# CRL-1573
immortalized brown adipocytes	Kahn et al.[55]	N/A
3T3-LA preadipocytes	Thiele et al.[56]	N/A
Experimental models: Organisms/strains		
Adipoq-CreERT2: C57BL/6-Tg (Adipoq-icre/ERT2)1Soff/J	Wolfrum et al.[57]	N/A
Medag$^{fl/fl}$: C57BL/6N-Atm1Brd Medagtm2a(KOMP)Wtsi/Mmucd	MMRRC	Cat# 048575-UCD
Adipoq-CreERT2 X Medag$^{fl/fl}$	Christian Wolfrum	This paper
Oligonucleotides		
qPCR primers	Microsynth	Listed in Table S2
siRNAs	Microsynth	Listed in Table S1
Primers for molecular cloning	Microsynth	Listed in Table S3
Recombinant DNA		
plenti-PKA-RIIβ-V5	Christian Wolfrum	This paper
pLenti-PKA-Cα-HA	Christian Wolfrum	This paper
plenti-MEDAG^{wildtype}-FLAG	Christian Wolfrum	This paper
plenti-MEDAG^{251A}-FLAG	Christian Wolfrum	This paper
plenti-MEDAG^{251D}-FLAG	Christian Wolfrum	This paper
pMD2.G	Turelli et al.[58]	Didier Trono Addgene plasmid Cat# 12259
psPAX2	Turelli et al.[58]	Didier Trono Addgene plasmid Cat# 12260
pLenti-CMV-MCS-BSD vector	Witwicka et al.[59]	Paul Odgren Addgene plasmid Cat# 73582
Software and algorithms		
ImageJ	NIH, USA	https://imagej.net/ij/

(*Continued on next page*)

CellPress
OPEN ACCESS

Continued

REAGENT or RESOURCE	SOURCE	IDENTIFIER
Phenomaster software version 5.6.5	TSE systems	https://www.tse-systems.com/products/phenomaster/?utm_term=metabolic%20cage&utm_campaign=Phenomaster+Academia&utm_source=adwords&utm_medium=ppc&hsa_acc=6040599756&hsa_cam=21247035327&hsa_grp=162182839575&hsa_ad=698298237521&hsa_src=g&hsa_tgt=kwd-2379065883768&hsa_kw=metabolic%20cage&hsa_mt=b&hsa_net=adwords&hsa_ver=3&gad_source=1&gad_campaignid=21247035327&gbraid=0AAAAADviuB4kszurM7y2-30g5VC3kc0QF&gclid=Cj0KCQiAosrJBhD0ARIsAHebCNq5Vil-eiK2eU89LyTh_vfMbIQk7Grev99tTjOup3rKynMVybx6mUEaAnFREALw_wcB
Wave - XF96 software version 2.3.0.19	Agilent	https://www.agilent.com/en/product/cell-analysis/real-time-cell-metabolic-analysis/xf-software/seahorse-wave-desktop-software-740897
ImageQuant LAS 4000 version 1.1	GE Healthcare	N/A
ViiA7 software version 1.2.3	Applied Biosystems	https://www.thermofisher.com/ch/en/home/technical-resources/software-downloads/applied-biosystems-viia-7-real-time-pcr-system.html
Gen5 version 1.10	BioTek	https://www.agilent.com/en/product/microplate-instrumentation/microplate-instrumentation-control-analysis-software/imager-reader-control-analysis-software/biotek-gen5-software-for-detection-1623227?srsltid=AfmBOorCmgClQTOuznCAuejMVsuTvR8soq5eFCCwR4Wu8hGufqI1njik#tools
Graphical Abstract	Biorender	https://www.biorender.com/
GraphPad Prism 10	GraphPad software	https://www.graphpad.com/
Resource website for human cohort 4	Reinisch et al.[30]	https://github.com/WolfrumLab/MHUO

EXPERIMENTAL MODEL AND STUDY PARTICIPANT DETAILS

Clinical sample acquisition of human adipose tissue

For human cohort 1, to quantify *MEDAG* expression in human adipose tissue, we analyzed transcriptomes of paired deep neck BAT and subcutaneous WAT biopsies of 44 patients undergoing neck surgery. The clinical study was approved by the Local Ethics Committee (University Hospital in Bratislava, Slovakia) and it conforms to the ethical guidelines of the 2000 Helsinki declaration. All study participants provided witnessed written informed consent prior to entering the study. Deep neck adipose tissue samples were obtained from the lower third of the neck by an experienced ENT surgeon from 44 individuals (12 Male/32 Female) during neck surgery under general anesthesia, age (age=45.68 ± 16 yrs, BMI= 25.52 ± 4.15 kg/m^2). The deep neck adipose tissue sample was taken from pre- and paravertebral space between the common carotid and trachea in case of thyroid surgery and just laterally to the carotid sheath in case of branchial cleft cyst surgery. In all cases, the surgical approach was sufficient to reach and sample the deep neck adipose tissue without any additional morbidity. Patients with malignant disease and subjects younger than 18 years were excluded from participation in the study. All participants self-identified as White/Caucasuan. Correlation analyses between clinical parameters and study variables were performed in the full cohort and were not adjusted for sex and not stratified by sex.

For human cohort 2, *MEDAG* expression and paired clinical parameters were obtained from a previously published clinical trial (ClinicalTrials.gov ID: NCT03269747) that investigated the effects of high-dose glucocorticoid treatment on brown adipose tissue activity in humans.[27] The study protocol of the interventional trial in healthy volunteers was approved by the regional ethics committee (Ethik-Kommission Nordwest-und Zentralschweiz) at the University of Basel (EKNZ 2016-01859). The study was conducted according to the Declaration of Helsinki and ICH-GCP. Participants provided written informed consent before taking part in any study related procedures. 16 healthy individuals (16 Males) were recruited, and the study was performed in Basel, Switzerland. In 15 of the 16

participants, biopsies were sampled from the supraclavicular adipose tissue depot. All participants self-identified as White/Caucasuan. Correlation analyses between clinical parameters and study variables were performed in the full cohort and were not adjusted for sex and not stratified by sex.

For human cohort 3, subcutaneous WAT samples and paired clinical parameters were obtained from ACTIBATE randomized controlled trial (ClinicalTrials.gov ID: NCT02365129).[28,60] The Human Research Ethics Committee of both University of Granada (n° 924) and Servicio Andaluz de Salud (Centro de Granada, CEI-Granada) approved the study design, study protocols and informed consent procedure. All participants provided a written informed consent. 150 sedentary, healthy, young adults (50% women) aged 18–25 years were recruited. *MEDAG* expression and paired clinical parameters were analyzed from 61 individuals (13 Males/48 Female). All participants self-identified as White/Caucasuan. Correlation analyses between clinical parameters and study variables were performed in the full cohort and were not adjusted for sex and not stratified by sex.

For human cohort 4, bulk and snRNAseq data were used from the metabolically healthy and unhealthy cohort of Leipzig Obesity Biobank (LOBB, https://www.helmholtz-munich.de/en/hi-mag/cohort/leipzig-obesity-bio-bank-lobb). The study was performed in agreement with the Declaration of Helsinki and approved by the Ethics Committee of the University of Leipzig (approval numbers 159-12-21052012, 017-12-23012012). Samples were only collected from adult male and female individuals who have provided written informed consent. This cohort included 32 insulin-sensitive individuals (71.8% female; age: 38.75 ± 10.98 years; BMI: 46 ± 6.82 kg/m^2) and 45 insulin-resistant individuals (71.1% female; age: 47.09 ± 7.49 years; BMI: 46.89 ± 8.12 kg/m^2) with obesity. *MEDAG* expression and paired clinical parameters were analyzed from 68 individuals (18 Males/50 Female). All participants self-identified as White/Caucasuan. Correlation analyses between clinical parameters and study variables were performed in the full cohort and were not adjusted for sex and not stratified by sex.

Mice experiments

All animal procedures were approved by the Veterinary office of the Canton of Zurich. Sample size was determined based on previous experiments in our lab and similar studies reported in the literature. All mice used for the experiments were male, housed 3-4 littermates per cage in individually ventilated cages at standard housing conditions (22°C, 12 h reversed light/dark cycle, dark phase starting at 7am), with ad libitum access to chow (18 % proteins, 4.5 % fibers, 4.5 % fat, 6.3 % ashes, Provimi Kliba SA) and water. Health status of all mouse lines was regularly monitored according to FELASA guidelines. Only male mice were used in this study; therefore, sex-dependent effects were not assessed.

MEDAGfl/fl mouse strain used for this research project was created by MMRRC (ID:048575-UCD, Mutant Mouse Resource & Research Centers supported by NIH). Conditional allele was achieved via flippase (Flp) recombination of knockout first allele. Flp deleter mouse was kindly provided by Prof. Markus Stoffel (ETH Zurich). Inducible adipocyte specific ablation of MEDAG was completed after crossing MEDAGfl/fl mice to AdipCreERT2[57] mice. For the high-fat diet (HFD) cohorts, male mice aged 8 weeks underwent oral gavage of tamoxifen (2 mg/day in sunflower oil, Sigma-Aldrich) to induce recombination of the floxed allele. After 2-week washout period of tamoxifen, these mice were fed a high-fat diet (23.9% protein, 4.9% fiber, 35% fat, and 5.0% ash, provided by Provimi Kliba SA) for a period of 12 weeks. A booster regimen (2 mg/day tamoxifen) was administered by oral gavage on three consecutive days during Week 6 of HFD to ensure sustained recombination efficiency. For the chow diet cohorts, recombination of the floxed alleles was performed using tamoxifen in male mice aged 10–12 weeks, followed by a 2-week washout period of tamoxifen prior to conducting subsequent metabolic studies.

Cell culture-immortalized murine brown adipocytes

Preadipocytes isolated from the stromal-vascular fraction of interscapular brown adipose tissue (iBAT) of late fetal and newborn C57Bl/6 mice (both sexes) and immortalized through the introduction of the SV40 antigen were generously provided by Prof. Klein.[55] Preadipocytes (between passage 4 and 6) were cultured on collagen-coated plates in DMEM supplemented with 10% FBS and 1% Penicillin/Streptomycin (Gibco) in a normoxic humidified incubator maintained at 5% CO2 and 37°C. Upon reaching confluence, adipogenic differentiation was initiated by adding IBMX (500 μM), dexamethasone (1 μM), insulin (20 nM), T3 (1 nM), and indomethacin (125 μM) to the medium. All reagents were procured from Sigma-Aldrich. After 48 hours, the differentiation medium was replaced with fresh maintenance medium containing insulin and T3, which was refreshed every other day. differentiating adipocytes on day 5 were trypsinized, counted, and replated onto collagen-coated multi-well plates to lower cell density. Following replating, cells were allowed to attach, recover, and mature before undergoing siRNA transfection with 100 nM siRNA pools on day 6. Cells were collected on day 9 for RNA, protein analysis, measurements of cellular respiration, and other assessments. All siRNA sequences are listed in Table S1. Throughout the course of this study, all cell lines used were regularly tested negative for mycoplasma contamination.

Cell culture-3T3-L1

3T3-L1 preadipocytes (ATCC CL-173, kindly provided by Prof. Thiele[56]) were maintained in growth medium (DMEM 4.5 g l−1 glucose, 10% FCS plus penicillin/streptomycin) at 5% CO2 and 37°C. For differentiation, cells were seeded into 48-well plates. After 24 h, differentiation was initiated (day 0) by replacing the medium with induction cocktail containing 1 μM rosiglitazone, 10 μg/ml insulin, 10 μM dexamethasone and 0.5 mM 3-isobutyl-1-methylxanthine for 2 days. Cells were then maintained in growth medium with insulin only for 2–4 days, with media replacement every 48 h. Differentiation progression was assessed daily via phase-contrast

CellPress
OPEN ACCESS

microscopy to monitor intracellular lipid droplet accumulation. On day 6 post-induction, cells were transfected with 100 nM siRNA pools accordingly. Cells were harvested on day 9 post-induction for RNA and protein analysis.

METHOD DETAILS

Clinical transcriptome study cohorts

For human cohort 1, Adipose tissue samples were immediately cleaned from blood and connective tissue, and frozen in liquid nitrogen until further processing. rRNA-depleted RNA-sequencing data were prepared on the basis of the SMARTseq protocol.[61] Briefly, isolated RNA was treated with DNaseI and reverse transcribed using an oligo(dT) and a template switch oligo. cDNA was amplified using ISPCR primers and tagmentated with Tn5 using the Nextera DNA Flex kit (Illumina, San Diego, CA). All libraries were sequenced on a Novaseq 6000 instrument at Functional Genomics Center Zurich. The raw reads were first cleaned by removing adapter sequences and poly-x sequences (> 9 nt used for detection) using fastp (version 0.20.0). Reads with length <18nt after trimming were additionally filtered out. Sequence pseudo alignment of the resulting high-quality reads to the Human reference genome (build GRCh38.p13) and quantification of gene level expression (gene model definition from GENCODE release 32) was carried out using Kallisto v0.46.1. Samples with counts exceeding 20 million were subsequently down-sampled. Down-sampled raw counts were homoscedastically normalized with respect to the library size and differential gene expression analysis was performed with subject being the covariate using the R package DESeq2 v1.44.0.

For human cohort 2, the description of the cohort and the data analysis are described previously.[27] In brief, total RNA was extracted from brown adipose tissue samples with TRI Reagent (Invitrogen), accordingly to the manufacturer's instructions. All libraries were sequenced on a Novaseq 6000 instrument. Adapter sequences and low-quality bases were trimmed off from the raw reads using fastp v0.20 for quality control. Filtered high-quality reads were mapped against the human reference genome assembly (build GRCh38. p13) using STAR v2.7.4a. Gene expression values were quantified using the R package Rsubread v2.2.4 and genes were considered to be present if they had at least 10 counts in half of the samples. Differential gene expression analysis was performed using the R package edgeR v3.34.

For human cohort 3, The BRB-seq libraries were prepared at Alithea Genomics Laboratory in Epalinges, Switzerland, according to the following protocols. For the MERCURIUS BRB-seq library preparation service, RNA samples were shipped on dry ice and underwent quantification and quality control (QC) before reverse transcription. Depending on the number of samples, the RT was carried out in batches of either 96 or 384, utilising a set of barcoded oligo-dT primers from BRB-seq kits (96-sample BRB-seq kit, PN10813; 384-sample BRB-seq kit, PN11013; Alithea Genomics) accordingly. The cDNA was pooled into a single tube, column-purified and subjected to ExoI treatment before proceeding with cDNA second strand synthesis. The Illumina-compatible Unique Dual Indexed (UDI) library was prepared, and the libraries were sequenced on the Illumina NovaSeq instrument, as previously detailed.[62] The FASTQ files were then sample-demultiplexed and aligned to the reference genome using STARsolo version 2.7.9a. The resulting read count matrices were subsequently used for downstream gene expression analysis.

For human cohort 4, the description of the cohort and the data analysis are described previously.[30] Briefly, rRNA-depleted RNA-sequencing data were prepared on the basis of the SMARTseq protocol.[61] Isolated RNA was treated with DNaseI and reverse transcribed using an oligo(dT) and a template switch oligo. cDNA was amplified using ISPCR primers and tagmentated with Tn5 using the Nextera DNA Flex kit (Illumina, San Diego, CA). All libraries were sequenced on a Novaseq 6000 instrument at Functional Genomics Center Zurich. Samples with counts exceeding 20 million were subsequently down-sampled. Down-sampled raw counts were homoscedastically normalized with respect to the library size and differential gene expression analysis was performed with subject being the covariate using the R package DESeq2 v1.44.0. Normalized counts were adjusted for exon mapping rate using the R package limma v3.60.2 for quality control. For snRNA-seq sequencing, frozen tissues were used for nuclei isolation, followed by 10X-based library preparation according to manufacturer's protocol (10X genomics, Pleasanton, CA, United States). The libraries were sequenced on a Novaseq6000 instrument (Illumina, Eindhoven, Netherlands) at health 2030 genome center. The R package Seurat v4.4.0 was used to process and analyze filtered feature-barcode count matrices. For quality control, nuclei with unique feature counts <300 or >5000, UMI counts > 20,000 and mitochondrial gene counts >5% were discarded from downstream analysis. The Cell Ranger v.7.1.0 pipeline was used for sample demultiplexing, read alignment against reference genome assembly GRCh38, cell barcode processing and unique molecular identifier counting. MEDAG expression was queried using the web applications provided in https://github.com/WolfrumLab/MHUO.

Intraperitoneal Glucose Tolerance Test

To measure glucose tolerance, mice were fasted for 6 hours by removal to a clean cage without food at the end of the dark (active) phase. Mice were weighed and fasting glucose levels were obtained from a small tail clip using a standard glucometer (ACCU-CHEK Aviva, Roche), D-glucose (2 g/kg body weight, Sigma-Aldrich) was injected intraperitoneally. Blood glucose levels were measured 0, 15, 30, 45, 60 and 120 minutes after glucose injection using glucometer.

Intraperitoneal Insulin Tolerance Test

To measure insulin tolerance, mice were fasted for 6 hours by removal to a clean cage without food at the end of the dark (active) phase. Mice were weighed and fasting glucose levels were obtained from a small tail clip using a standard glucometer

(ACCU-CHEK Aviva, Roche), Insulin (1 U/kg body weight) was injected intraperitoneally. Blood glucose levels were measured 0, 15, 30, 45, 60 and 120 minutes after insulin injection using glucometer.

Body composition measurement

Liver mice body composition was measured with a magnetic resonance imaging technique (EchoMRI 130, Echo Medical Systems). Mice were placed in a manufacturer-supplied restrainer (without anesthesia) and scanned according to the manufacturer's instructions. Each mouse was scanned using the instrument's standard mouse setting. Fat and lean mass was analyzed using Echo MRI 14 software.

Indirect Calorimetry

Indirect calorimetry measurements were performed with the Phenomaster (TSE Systems) using TSE PhenoMaster software v5.6.5 according to the manufacturer's guidelines. O2 and CO2 levels were measured for 60s every 13 minutes continuously. Energy expenditure was calculated according to the manufacturer's guidelines. The respiratory quotient was estimated by calculating the ratio of CO2 production to O2 consumption. Animals were single-caged and acclimated to the metabolic cage for 48 hours prior metabolic recording. Locomotor activity, food and water intake were monitored throughout the whole measurement. Following basal measurement at thermoneutrality (28°C), the mice were exposed to 22°C and then to 8°C, or injected intraperitoneally with CL316,243 (0.1 mg/kg/day) to activate non-shivering thermogenesis.

Tissue Harvest

Animals were individually euthanized in a carbon dioxide environment. Following euthanasia, all tissues were meticulously dissected, weighed, and immediately snap-frozen in liquid nitrogen for subsequent processing. Popliteal lymph nodes were carefully excised from the inguinal white adipose tissue (iWAT) for gene and protein expression analyses. For the isolation of RNA and proteins, the entire adipose tissue depot was homogenized.

Cellular Respiration and Glycolytic Stress Test

For the measurement of cellular respiration, immortalized murine brown adipocytes were cultured on collagen-coated cell culture dishes. On day 5 of differentiation, adipocytes were trypsinized and replated at a density of 7,000 cells per well, allowing them to recover for 48 hours prior to treatment. Since hMADS cells grow in a monolayer, they were differentiated directly on collagen-coated 96-well Seahorse microplates. On the day of experiment, adipogenic medium was replaced with XF Assay Medium (pH 7.4, Seahorse Bioscience) supplemented with glucose (1 g/L; Sigma-Aldrich), 2 mM sodium pyruvate (Invitrogen) and 2 mM L-GLUTamine (Invitrogen). The oxygen consumption rate (OCR) was measured using the Extracellular flux analyzer XF96 (Agilent). Test compounds were sequentially injected to obtain following concentrations: 1 mg/ml Oligomycin, 1 mM isoproterenol, (0.5 mM dibutyryl cAMP for hMADS), 1 mg/ml FCCP, 3 mM Rotenone with 2 mg/ml Antimycin A. OCR levels (pmol/min) were normalized to protein amount per well (μg protein). Non-mitochondrial respiration was subtracted to obtain basal, basal uncoupled, basal uncoupled, stimulated and maximal mitochondrial respiration.

For glycolytic stress test, on the day of experiment, adipogenic medium was replaced with XF Assay Medium (pH 7.4, Seahorse Bioscience) supplemented with 2 mM L-GLUTamine (Invitrogen). ECAR was measured using the Extracellular flux analyzer XF96 (Agilent). Test compounds were sequentially injected to obtain following concentrations: 70 mM D-Glucose, 1 mg/ml Oligomycin, 900 mM 2-DeoxyGlucose. ECAR values (mpH/min) were normalized to protein amount per well (μg protein). Non-glycolytic acidification was subtracted to obtain glycolysis, glycolytic capacity, and glycolytic reserve.

For the fuel dependency assessment, iBAs were differentiated in collagen-coated 96-well Seahorse microplates. On the assay day, cells were equilibrated for 1 h in XF assay medium (pH 7.4, Seahorse Bioscience) supplemented with 10 mM glucose (Sigma-Aldrich), 1 mM sodium pyruvate (Invitrogen) and 2 mM L-glutamine (Invitrogen). Mitochondrial substrate dependency was quantified through sequential injection of three metabolic inhibitors: 100 μM etomoxir (Sigma-Aldrich) to inhibit CPT1a-mediated fatty acid oxidation, 6 μM BPTES (Sigma-Aldrich) to suppress glutaminolysis via glutaminase inhibition, and 2 μM UK5099 (Sigma-Aldrich) to block mitochondrial pyruvate transport. Fuel-specific oxidative capacity was calculated as the percentage ratio: [(basal OCR - OCR after single inhibitor injection) / (basal OCR - OCR after double inhibitor injection)] $\times$ 100, where single inhibitor injection refers to administration of the pathway-specific inhibitor, and double inhibitor injection denotes co-administration of all remaining inhibitors.

Lipolysis

Lipolytic activity of mature brown adipocytes was determined as glycerol and free fatty acids release into culture media. Briefly, the cells were starved for 2 hours in low-glucose medium (Gibco) prior to analysis. Isoproterenol (1 μM; Sigma-Aldrich) was added and plate was incubated for another 30 mins or 1 hour at 37°C in humidified CO2 incubator. Media were collected and spun down to pellet detached cells. Glycerol and free fatty acid were assessed in the supernatant using the Glycerol reagent (Sigma-Aldrich) and NEFA assay kit (Wako NEFA KIT) respectively, according to manufacturer's instructions and normalized to protein content in the well.

CellPress
OPEN ACCESS

RNA extraction, cDNA synthesis, Quantitative RT-PCR

Total RNA was extracted from tissues or cells using Trizol reagent (Invitrogen) according to the manufacturer's instructions. DNase treatment (NEB BioLabs) was included to remove traces of genomic DNA. Reverse transcription was performed to generate cDNA library by using the High-Capacity cDNA Reverse transcription kit (Applied Biosystems), with 1mg of RNA. Quantitative PCR was performed on a ViiA7 (Applied Biosystems) and relative mRNA concentrations normalized to the expression of TBP were calculated by the ΔΔCt method. Primer sequences are listed in Table S2.

Protein extraction and western blot

Adipose tissue samples and in vitro differentiated adipocytes were homogenized in RIPA buffer (50 mM Tris-HCl pH 7.4, 150 mM NaCl, 2 mM EDTA, 1.0% Triton X100, 0.5% sodium deoxycholate) supplemented with protease inhibitor (Complete, Roche) and phosphatase inhibitor (Halt phosphatase inhibitor cocktail, ThermoFisher). Lysates were cleared by centrifugation at 12,000g for 15 minutes at 4°C. Protein concentration of the supernatants was determined by DC Protein Assay (Bio-Rad). An equal amount of proteins (30 mg) were separated on 10% SDS-polyacrylamide gel, transferred to a nitrocellulose membrane (Bio-Rad) and blotted by different antibodies. The primary antibody signal was visualized by horseradish peroxidase-conjugated secondary antibodies (1:8,000, Millipore) and the ImageQuant system (GE Healthcare Life Sciences). SuperSep™ Phos-tag™ precast gels (Fujifilm) were used to enable isolation of phosphorylated proteins by the level of phosphorylation.

Molecular cloning

Mouse Flag-MEDAG, HA-PKA-Cα, V5-PKA-RIIβ constructs were cloned from mouse cDNA library and inserted into pLenti-CMV-MCS-DBSD vector[59] to obtain pLenti-Flag-MEDAG, pLenti- HA-PKA-Cα, pLenti-V5-PKA-RIIβ construct. For mouse MEDAG mutant, we designed primers to replace Ser 251 to Ala 251 or Asp 251 to obtain Flag-MEDAG^{S251A} or Flag-MEDAG^{S251D}, and the CDS was then inserted into pLenti-CMV-MCS-DBSD vector to obtain pLenti-Flag- MEDAG^{S251A}. All the plasmids for cell culture work were extracted by NucleoBond Xtra-Midi kit (Macherey-Nagel). All primers used for molecular cloning were listed in Table S3.

Lentivirus packaging

For lentivirus packaging, the target plasmids were transfected into HEK293T cells together with pMD2.G (Addgene, 12259) and psPAX2 (Addgene, 12260)[58] by polyethylenimine in OptiMEM medium. The virus-containing medium was collected and concentrated in PEG-it Virus Precipitation Solution (SBI, LV825A-1) according to the manufacturer's instructions. The lentivirus transfection with/without siRNA transfection were performed on day 6 of iBAs culture.

CO- Immunoprecipitation (CO-IP)

For immunoprecipitation, iBAs were homogenized in RIPA buffer (50 mM Tris–HCl pH 7.4, 150 mM NaCl, 2 mM EDTA and 1.0% Triton X-100) with protease inhibitors (Complete, Roche) and phosphatase inhibitors (Halt phosphatase inhibitor cocktail, ThermoFisher). The homogenates were centrifuged at 12,000g for 10 min at 4 °C to collect cell lysates. After three washes with cold RIPA buffer, 20 μl Anti-Flag beads or Anti-V5 beads was added to cell lysates for overnight incubation with rotation at 4°C. The beads were then washed six times by cold RIPA buffer. The proteins were eluted by boiling the beads at 95°C for 5 min with 2x Lammeli buffer. The eluted protein was then analyzed by immunoblotting.

Dot blot overlay assay

Dot blot protein overlay assay was performed as described previously.[63] FLAG-MEDAG (WT), FLAG-MEDAG^{S251A}, and V5-PKA-RIIβ were expressed in HEK293 cells and lysed in a high-stringency buffer (50 mM Tris–HCl pH 7.4–7.5, 500 mM NaCl, 1% NP-40, 0.1% sodium deoxycholate, 1 mM EDTA, 10% glycerol, 1 mM DTT, protease inhibitors) to minimize indirect or weak associations and thereby improve sample purity. Recombinant protein was purified by immunoaffinity-capture via anti-V5 or anti-Flag conjugated resins and eluted under native conditions using the cognate epitope peptide (3×FLAG or V5). Residual peptide was removed by rapid buffer exchange using Zeba™ Spin Desalting Columns, 7K MWCO (Thermo Scientific) prior to the in-vitro association assays. The immunoaffinity-purified proteins were analyzed by SDS-PAGE followed by Coomassie Brilliant Blue staining (Figure S3E). Prominent bands at the expected molecular weights indicate the purity and integrity of the proteins used for in vitro protein–protein interaction assays. Using a vacuum manifold (Bio-Dot® apparatus), 10 μL of each protein was applied directly onto a nitrocellulose membrane. Membranes were air-dried for 10 min at room temperature to ensure protein adherence. Membranes were incubated in 5% BSA for 2 h at room temperature with gentle agitation to prevent non-specific binding. Blocked membranes were incubated overnight at 4°C with gentle shaking in probing buffer (TBST + 5% BSA) containing the purified, tagged "bait" protein. Unbound probe was removed by washing membranes 3× for 10 min each in TBST. Membranes were incubated with a primary antibody against the tag for 1 h at room temperature, washed 3× in TBST, incubated with HRP-conjugated secondary antibody (1:10,000) for 1 h, washed again, and developed using enhanced chemiluminescence (ECL) substrate.

Immunofluorescence

To immunostain MEDAG, PKA-Cα and PKA-RIIβ, iBAs were transfected with corresponding lentivirus. iBAs were fixed with 4% PFA for 20 mins and permeabilized by 0.25% PBST (Triton X-100 in PBS) for 20 mins. After three washes with cold PBS, cells were

blocked by 1% BSA for 1 h and incubated with primary antibodies overnight at 4°C. After three washes with cold PBS, cells were incubated with Alexa Fluor 488/568 conjugated secondary antibody (1:200, ThermoFisher) for 1 h at room temperature. Finally, cells were stained by Hoechst 33342 to label nuclei after three washes with PBS to remove residual secondary antibody. The pictures were all obtained by Olympus FluoView 3000 confocal microscope and processed by ImageJ. Co-localization was quantified using the Coloc2 plugin in Fiji/ImageJ.

Computational prediction of MEDAG-PKA-RIIβ dimer complex structure

Computational simulation was conducted to predict the complex structure of mouse PKA- RIIβ dimer and MEDAG using AlphaFold 3 web server (https://alphafoldserver.com/).[64] Both amino acid sequences of PKA- RIIβ dimer and MEDAG were obtained from Uniprot (Uniprot ID of PKA- RIIβ: H3BK84; Uniprot ID of MEDAG: Q14BA6). The copy number of PKA- RIIβ was set to 2 while the copy number of MEDAG was set to 1 for simulating a dimer-monomer interaction. To simulate a post-translational modification (PTM) of a specific residue (in this study, pSer251), the desired PTM was added to the target residue by the built-in toolbox of the server. Five complex structures were generated during the simulation and the most appropriate model was manually evaluated and selected. The molecular graphic figure was generated by PyMOL v.2.5.2 (Schrödinger, New using York, NY, USA).

Histological staining

Adipose tissues were fixed in 4% PFA for 24 h directly after tissue collection. To perform haematoxylin and eosin (H&E) staining, tissue pieces were transferred to 65% ethanol and embedded in paraffin in tissue processing machine and embedding machine, followed by section at 10 μm and staining using the standard protocol. Specifically, sections were deparaffinized in xylene (2 × 5 min) and rehydrated through a graded ethanol series (100%, 95%, 70%; 2-3 min each) to distilled water. Sections were stained in hematoxylin for 3-5 min and rinsed in running tap water for 5 min, followed by bluing in Scott's solution for 30-60 s. Sections were then counterstained in eosin Y for 30-90 s, rinsed quickly in water, dehydrated through graded ethanols (70%, 95%, 100%), cleared in xylene (2 × 5 min), and coverslipped using a xylene-based mounting medium. H&E-stained sections were imaged on a whole-slide scanner under identical illumination and acquisition settings across experimental groups. Adipocyte size was quantified in a blinded manner using ImageJ.

Plasma TG, FFA and cholesterol measurements

The blood samples were collected by cardiac puncture into EDTA-coated tubes after 4 h of fasting. Plasma was obtained by centrifugation at 8,000g for 20 min at 4°C. Plasma TG levels were determined using the TG assay kit (SPINREACT), and total cholesterol levels were measured with LabAssatTM Cholesterol kit (FUJIFILM). Plasma NEFA levels were determined using the NEFA assay kit (Wako NEFA kit).

cAMP levels and PKA kinase activity measurements

Cells were FBS-depleted for 2 hours prior to the cAMP assays in high glucose DMEM medium, followed by isoproterenol treatment for different timepoints. Prior to assay. Cells were briefly washed 1x with PBS. Subsequently, intracellular and tissue lysates cAMP concentration was measured using a cAMP Elisa kit (Enzo Life Sciences) according to manufacturer's instructions. Colorimetric assay was detected by SynergyMx plate reader (BioTek). cAMP levels (pmol) were normalized to protein amount per well (mg protein). Similarly, PKA kinase activity (ng) was measured using a PKA Kinase Activity kit (Enzo Life Sciences) according to manufacturer's instructions and normalized to protein amount per well (μg protein).

QUANTIFICATION AND STATISTICAL ANALYSIS

For in vivo studies, littermates were randomly assigned to treatment groups for all the experiments. Sample sizes were determined based on previous experiments using similar methodologies. The animal numbers used for all experiments are indicated in the corresponding figure legends. All animals were included in statistical analyses, and the investigators were not blinded. For cell culture experiments, biological replicates were no less than three (shown as n in the figure legends), and all cell culture experiments were performed with 2–3 technical replicates for RNA and protein analysis, 5–6 replicates for measurement of cellular respiration, and independently reproduced 2-4 times. Data are presented as mean ± SEM, when it is not indicated specifically. Two-tailed unpaired student's t-test was applied on comparison of two groups and two-way ANOVA with Tukey's post hoc multiple comparison test was applied on comparisons of multiple groups. Pearson or Spearman correlation coefficient was calculated to address association of two parameters. All statistical analyses were performed using GraphPad Prism 10. Statistical differences are indicated as * for $P < 0.05$, ** for $P < 0.01$, *** for $P < 0.001$ and **** for $P < 0.0001$.

Molecular Cell, Volume *86*

Supplemental information

MEDAG functions as an A-kinase-anchoring protein in adipocytes

Fen Long, Adhideb Ghosh, Tianyu Xu, Lianggong Ding, Chunyan Wu, Radhika Khandelwal, Falko Noé, Wenfei Sun, Hua Dong, Tongtong Wang, Anne Hoffmann, Vincent Gardeux, Bart Deplancke, Laith Abu-Nawwas, Patrik Stefanicka, Lukas Varga, Jonatan R. Ruiz, Matthias Blüher, Miroslav Balaz, Anand Kumar Sharma, and Christian Wolfrum

Supplementary figures and legends

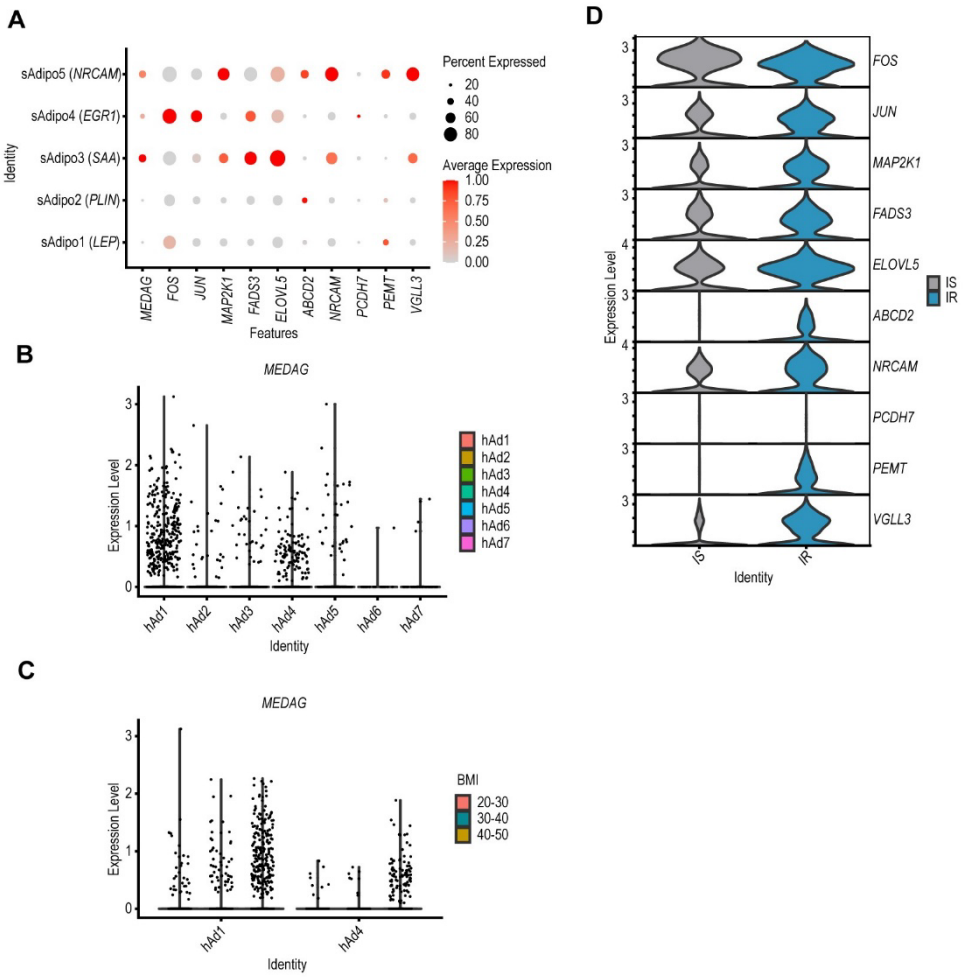

Figure S1. Adipose tissue *MEDAG* expression positively correlates with obesity and metabolic dysfunction in humans, related to Figure 1

(A) Dot plots showing expression of *MEDAG* and top marker genes within hAd1 and hAd4 subpopulation (Emont et al. dataset) in subcutaneous adipocyte subpopulations in human cohort 4.

(B) Expression of *MEDAG* in subcutaneous adipocyte subpopulations from Emont et al. dataset.

(C) Expression of *MEDAG* within hAd1 and hAd4 subpopulation (Emont et al. dataset) in individuals with different BMI.

(D) Violin plots comparing *MEDAG* expression and the top five markers of hAd1 and hAd4 subpopulation (Emont et al. dataset) between metabolically healthy (IS) versus unhealthy (IR) human subcutaneous WAT in human cohort 4.

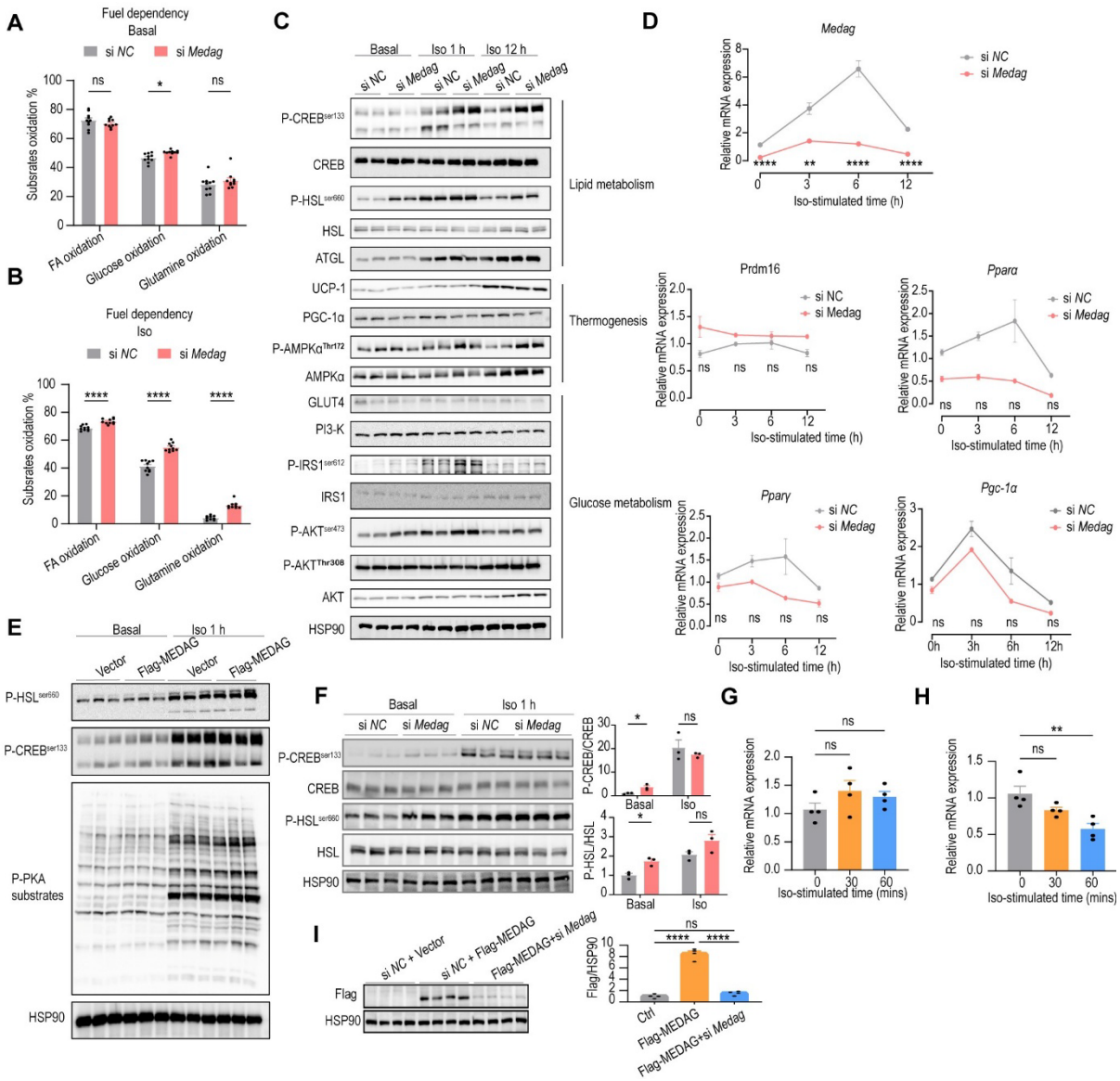

Figure S2. *Medag* regulates adipocyte respiration by PKA activity modulation, related to Figure 2

(A) Fuel dependency assay in iBAs with Medag knockdown (n=10).

(B) Fuel dependency assay in iBAs treated with 1 μM isoproterenol for 1 h after Medag knockdown (n=9-10 for each group).

(C) Representative blots of markers linked to lipid metabolism and glucose/insulin signaling, in iBAs treated with 1 μM isoproterenol for 1 h or 12 h after MEDAG knockdown (n = 2). Repeated independently three times with similar results.

(D) Real-time qPCR of thermogenesis markers in iBAs treated with 1 μM isoproterenol for different timepoints (n = 4).

(E) Representative blots of P-HSL, P-CREB and P-PKA substrates protein levels (n = 3). Repeated independently three times with similar results.

(F) Representative blots and quantification of Flag-MEDAG protein levels in iBAs with Flag-MEDAG overexpression following Medag knockdown (n = 4).

(G) Representative blots and quantification of P-HSL and P-CREB protein levels in 3T3 treated with 10 μM isoproterenol for 1 h after Medag knockdown (n = 3).

(H) Real-time qPCR of *Medag* in iBAs treated with 1 μM isoproterenol for different timepoints (n=4).

(I) Real-time qPCR of *Medag* in 3T3 treated with 10 μM isoproterenol for different timepoints (n=4).

Data are presented as mean ± SEM and analyzed using unpaired two-tailed t-test (A, B, D, G) and one-way ANOVA with Tukey's post hoc multiple comparison test (H, I). ns, not significant, **$p < 0.01$, ***$p < 0.001$, ****$p < 0.0001$.

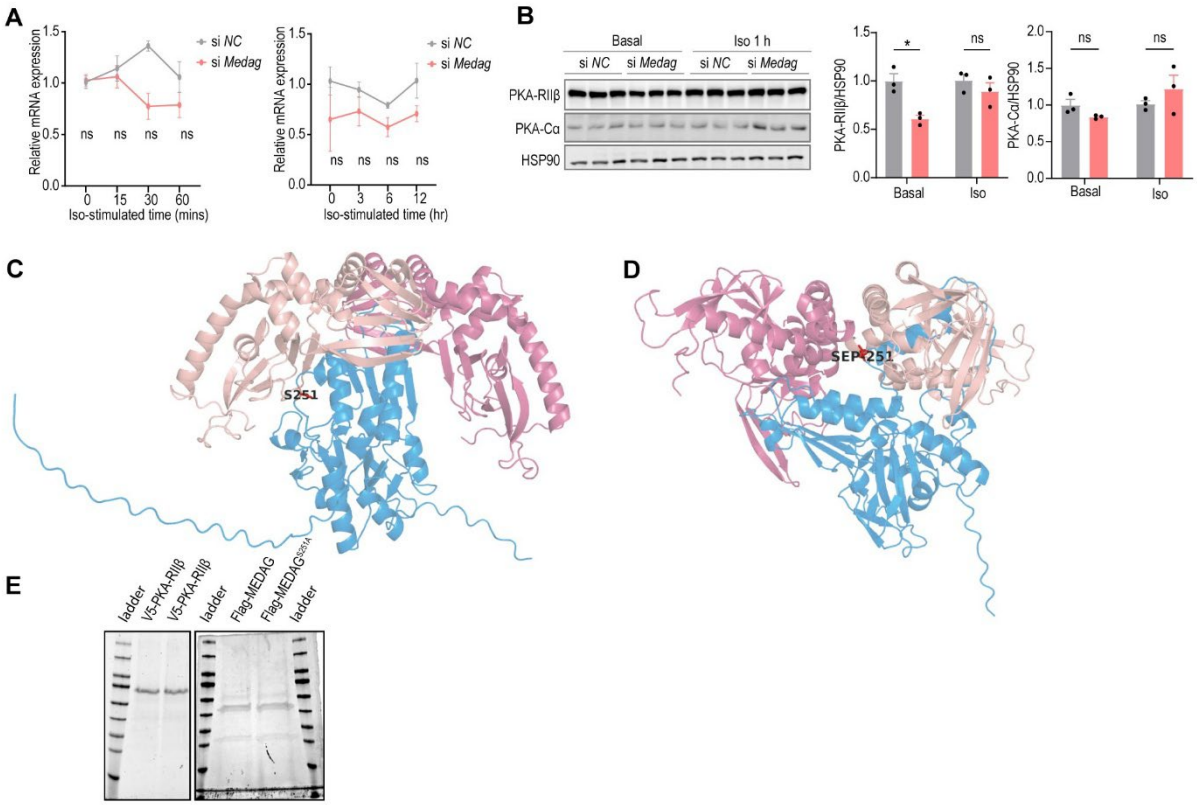

Figure S3. MEDAG regulates the stability of the PKA-RIIβ subunits, related to Figure 4

(A) Real-time qPCR of PKA-RIIβ in iBAs treated with 1 μM isoproterenol for different timepoints (n = 6).

(B) Representative blots and quantification of PKA-RIIβ protein levels in 3T3 under basal conditions and following 10 μM isoproterenol stimulation after Medag knockdown (n = 3).

(C) Computational predicted structure complex of WT-MEDAG with PKA-RIIβ dimer using Alphafold 3. The two dimers of PKA-RIIβ are labeled in Salmon and Warmpink while MEDAG is labeled in Marine.

(D) Computational predicted structure complex of Ser251 phospho-MEDAG with PKA-RIIβ dimer using Alphafold 3. The two dimers of PKA-RIIβ are labeled in Salmon and Warmpink while MEDAG is labeled in Marine.

(E) Coomassie Blue-stained SDS-PAGE showing immunoaffinity-purified V5-PKA-RIIβ, WT-MEDAG and Flag-MEDAG^{S251A}.

Data are presented as mean ± SEM and analyzed using unpaired two-tailed t-test (A, B). ns, not significant, *$p < 0.05$.

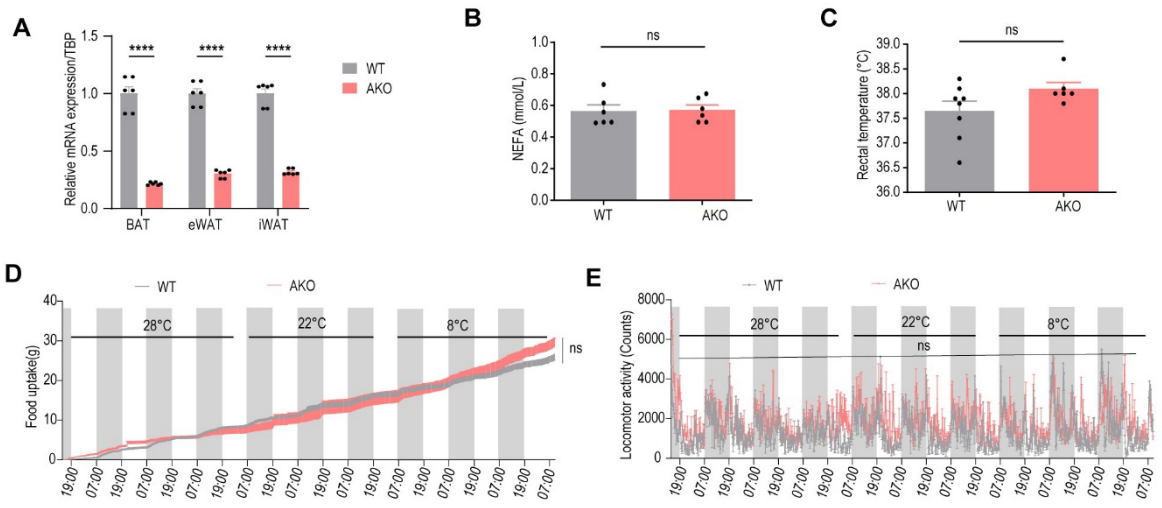

Figure S4. *Medag* AKO mice exhibit increased EE and are resistant to HFD-induced obesity, related to Figure 5

(A) *Medag* knockout efficiency in different adipose depots in AKO mice (n = 6).

(B) Plasma non-esterified fatty acids (NEFA) after 12 weeks of HFD feeding (n = 6).

(C) Rectal temperature of mice housed at 22°C (n = 8 for WT and 6 for AKO).

(D) Accumulative food uptake in mice throughout different temperature exposure at 28°C (S), 22°C (T), 8°C (U) (n = 5).

(E) Locomotor activity in mice throughout different temperature exposure at 28°C (S), 22°C (T), 8°C (U) (n = 5).

Data are presented as mean ± SEM. Each data point represents an individual animal. Statistical analysis was performed using unpaired two-tailed t-test (A-E). ns, not significant, ****$p < 0.0001$.

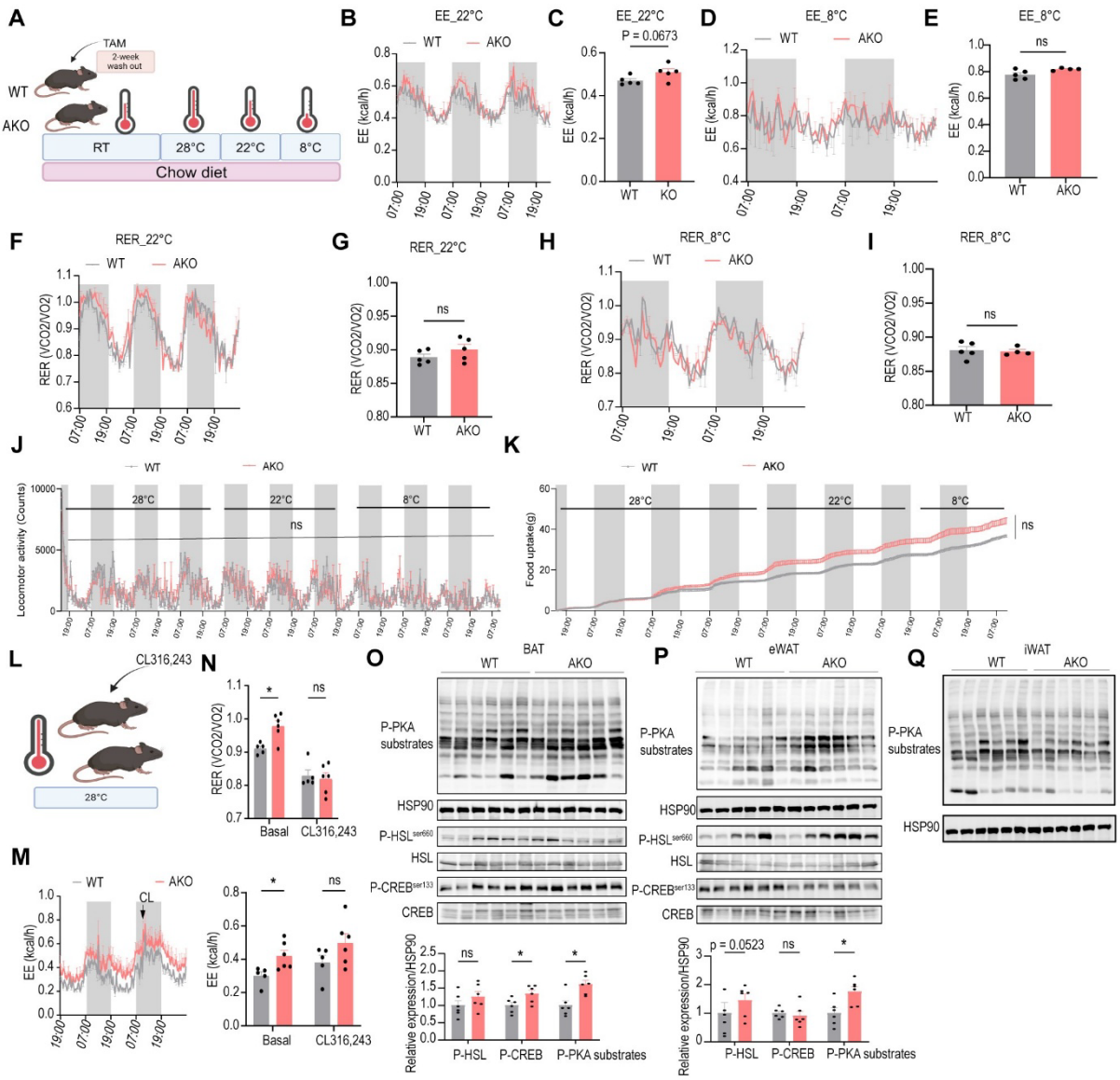

Figure S5. PPARγ/GLUT signaling acts downstream of PKA activation in *Medag* AKO mice, related to Figure 6

(A) Schematic illustration of experimental design: thermoneutral (28ºC), room temperature (22 ºC), and cold exposure (8 ºC).

(B-C) Energy expenditure curve (B) and daily energy expenditure (C) of mice housed at 22°C (n = 5).

(D-E) Energy expenditure curve (D) and daily energy expenditure (E) of mice housed at 8°C (n = 5 for WT and 4 for AKO).

(F-G) RER curve (F) and daily RER (G) of mice housed at 22°C (n = 5).

(H-I) RER curve (H) and daily RER (I) of mice housed at 8°C (n = 5 for WT and 4 for AKO).

(J) Locomotor activity in mice housed at 28°C (S), 22°C (T), 8°C (U) (n = 5 and n=4 for AKO when housed at 8°C).

(K) Accumulative food uptake in mice housed at 28°C (S), 22°C (T), 8°C (U) (n = 5 and n=4 for AKO when housed at 8°C).

(L) Scheme of experimental design.

(M) Energy expenditure mice housed at 28°C before and after CL316,243 injection (n = 5).

(N) RER of mice housed at 28°C before and after CL316,243 injection (n = 5).

(O) Representative blots and quantification of P-PKA substrates, P-HSL, and P-CREB protein levels in BAT from mice housed at 28°C for 1 week (n = 6).

(P) Representative blots and quantification of P-PKA substrates, P-HSL, and P-CREB protein levels in eWAT from mice housed at 28°C for 1 week (n = 6).

(Q) Representative blots of P-PKA substrates in iWAT of mice housed at 28°C for 1 week (n = 6).

Data are presented as mean ± SEM. Each data point represents an individual animal. Statistical analysis was performed using unpaired two-tailed t-test (C, E, G, I-P). ns, not significant, *$p < 0.05$.

Table S1. Sequence of siRNA pools used to knockdown genes in immortalized brown adipocytes (Mouse), related to STAR Methods

Gene symbol	Sense siRNA Sequence (5'-3')
Medag	#1 GGGAAACGATACTGAGCAA #2 GCAAACCTATGGTATTCTT #3 GCAGAATTCTCATTTCCAA
Praja2	#1 GUA GUA AGG CCC AAA GUU Aß #2 CGG CAA GAA UCU CGG GAC A #3 UGG AAG AAG ACA UGC GUA U

Table S2. Sequence of qPCR primers used in this study, related to STAR Methods

Gene symbol	Species	Primer Sequence (5'-3')
Medag	Mouse	Forward: ATCGCCTCAGCAGCTACATC Reverse: TGTCCTTCTTGGTCTGCACG
Prdm16	Mouse	Forward: CGCTTCGAATGTGAAAACTG Reverse: AAGGTCTTGCCACAGTCAGG
Cox7A1	Mouse	Forward: CAGCGTCATGGTCAGTCTGT Reverse: AGAAAACCGTGTGGCAGAGA
Elovl	Mouse	Forward: GGCATAATTGTTACCTGATTCAGG Reverse: GATGGTTCTGGGCACCATCTT
Pparα	Mouse	Forward: TCGGCGAACTATTCGGCTG Reverse: GCACTTGTGAAAACGGCAGT
Pparγ	Mouse	Forward: GTGGGGATAAAGCATCAGGC Reverse: CCGGCAGTTAAGATCACACCTA
Ucp-1	Mouse	Forward: CAGCCGGCTTAATGACTGGA Reverse: TGATCCCATGCAGATGGCTC
Pgc-1α	Mouse	Forward: CTCTCAGTAAGGGGCTGGTTG Reverse: CGAATGACGCCAGTCAAGC
Pkm2	Mouse	Forward: GTGGTGACCTGGGCATTGAG Reverse: GCACAGATGACAGGCTTCCC
Pepck	Mouse	Forward: CGGATGGGCATATCTGTGCT Reverse: AGGCCCAGTTGTTGACCAA
Glut4	Mouse	Forward: GACGGACACTCCATCTGTTG Reverse: GCCACGATGGAGACATAGC
PKA-RIIβ	Mouse	Forward: CTTTATCGAGTCCCTGCCGT Reverse: CAGACGCTGCTCTTGGTTTG

Table S3. Sequence of primers used for molecular cloning, related to STAR Methods

Plasmid	Primer Sequence (5'-3')
Flag-MEDAG	Forward: GGACTAGTATGGCCACTGCAGCGTGC Reverse: CGACGCGTTCACTTATCGTCGTCATCCTTGTAATCGATAAGTTGGCTGGATGTCT
HA-PKA-Cα	Forward: GGACTAGTGCCACCATGGGCAACGCCGCCGCCGC Reverse: CGACGCGTCTAGGCGTAGTCAGGCACGTCGTAAGGATAAAACTCAGTAAACTCCTTGCC
V5-PKA-RIIβ	Forward: GGACTAGTATGAGCATCGAGATCCCC Reverse: CGACGCGTTCAAGTAGAATCGAGACCGAGGAGAGGGTTAGGGATAGGCTTACCTCATGCAGTGGGCTCAAC
Flag-MEDAG^{S251A}	Forward: CTAATACGAAGGAGTGCTTTCTCTGATCGGAAA Reverse: TTTCCGATCAGAGAAACGACTCCTTCGTATTAG
Flag-MEDAG^{S251D}	Forward: CTAATACGAAGGAGTGATTTCTCTGATCGGAAA Reverse: TTTCCGATCAGAGAAAAGACTCCTTCGTATTAG